Manuscript (non-LaTeX)
Click here to download Manuscript (non-LaTeX): andes_waves_text.doc

A Modeling Study of Stratospheric Waves over the Southern Andes and Drake Passage

[1]Qingfang Jiang, [1]James D. Doyle, [1]Alex Reinecke, [2]Ronald B. Smith, and [3]Stephen D. Eckermann

[1] Naval Research Laboratory, Monterey, CA
[2]Department of Geology, Yale University, New Haven, CT
[3]Naval Research Laboratory, Washington, DC

Submitted to the Journal of Atmospheric Sciences for Consideration of Publication

June 2012

Corresponding author address:
Qingfang Jiang
Naval Research Laboratory
7 Grace Hopper Ave.
Monterey, CA 93940-5502
Email: jiang@nrlmry.navy.mil

ABSTRACT

Large-amplitude stratospheric waves over the southern Andes and Drake Passage were observed by AIRS on 8-9 August 2010 and were well captured by a numerical simulation using the COAMPS model. The simulated tropospheric waves are generated by flow over the high central Andes ridge and the Patagonian peaks in the southern Andes. Some waves emanating from Patagonia extend southeastward across Drake Passage in the stratosphere over a horizontal distance of more than a thousand kilometers. The wave momentum flux is characterized by a maximum over Patagonian peaks in the troposphere, which splits into two comparable maxima in the stratosphere; one right over the terrain and the other tilting southward with the altitude over Drake Passage.

Using a ray-tracing methodology based on linear theory and conditions derived from the numerical simulation, we find that waves that originate from the high ridge in Central Andes are absorbed by a critical level in the lower stratosphere. The three-dimensional waves originating from Patagonia could propagate equatorward and are absorbed by a critical level aloft, upward nearly vertically and break-down in the stratosphere and lower mesosphere, or polarward and form the observed linear stratospheric wave patterns oriented across the Drake Passage. The southward propagation assisted by wave fraction on account of meridional shear of zonal winds contributes to the missing orographic drag near 60^0 S.

1. Introduction

Gravity waves entering into the stratosphere and mesosphere play an important role in driving the general circulation, enhancing vertical mixing and contributing to polar stratospheric cloud formation, which has further implications for ozone depletion over Polar Regions (e.g., Carslaw et al. 1998). Over the past few decades, there have been numerous studies of gravity wave drag parameterizations in climate and general circulation models (see Kim et al. 2003; Fritts and Alexander 2003 for reviews). Major tropospheric gravity wave sources identified by previous studies include mountains, convection in tropical areas (Alexander and Vincent 2000), lower-tropospheric frontal activities, and upper-tropospheric unbalanced jet streams (Spiga et al. 2008), each of which has been the subject of extensive studies. Particularly, our knowledge of topographic waves over mid-latitude mountains have been significantly advanced through several large field campaigns conducted over major barriers such as the Rockies (Wave Momentum Flux Experiment (WAMFLEX), Lilly and Kennedy (1973)), the European Alps (Mesoscale Alpine Programme (MAP), see Smith et al. 2007 for a review), and the Sierras (Sierra Waves Project (SWP, 1954)), Terrain-Induced Rotor Experiment (T-REX), Grubišić et al. (2008)). Mountain waves over high-latitude areas, such as the southern Andes, received much less attention.

Over the past decade, the global distribution of gravity wave variances in the stratosphere have been examined by several studies using observations obtained by new satellite-borne sensors. A striking maximum in gravity wave variances or momentum fluxes was found over the southern tip of the Andes, Antarctic Peninsula and the Drake Passage (Jiang et al. 2002; Wu 2004; Alexander et al. 2008). Candidate wave sources

include topography (i.e., southern Andes and Antarctic Peninsula), jet-stream adjustment associated with strong baroclinicity near the 60^0S parallel, and polar vortex instability. For example, after examining 965 radiosonde soundings over 8 years launched from Rothera on the Antarctic Peninsula, Moffat-Griffin et al. (2011) concluded that the stratospheric gravity waves above Rothera are determined by a combination of up-going topographic waves and down-going waves originated from the edge of the polar vortex in the stratosphere. Plougonven et al. (2008) examined a wave breaking event over the Antarctic Peninsula using super-pressure balloon observations and mesoscale model simulations. They documented breaking waves in the lower stratosphere, which were generated by westerlies impinging on the Antarctic Peninsula. Stratospheric waves and wave drag were recently investigated by Shutts and Vosper (2011) using mesoscale and global model simulations. Gravity waves with a horizontal wavelength around 400 km were documented over southern Andes and Drake Passage in both the global and mesoscale model simulations. Nevertheless, compared to observations over mid-latitude terrain, comprehensive observations of waves over high-latitude terrain in the Southern Hemisphere are still rare.

This research is motivated by satellite images, which frequently reveal linear wave patterns over the southern Andes and the Drake Passage. The objectives of this study are three-folded. Firstly, we want to explore the capability of COAMPS in simulating stratospheric gravity waves by extending its model top from the previous capability at the 30 km level (i.e., lower stratosphere) to ~70 km ASL (i.e., lower mesosphere). Secondly, we want to advance our understanding of characteristics and dynamics of gravity waves over the southern Andes and Drake Passage through

examining the simulated waves. Furthermore, we expect that this case study will provide guidance for the planning of the Southern Andes-Antarctic Gravity-wave Initiative (SAANGRIA), which will be conducted over the southern Andes and Drake Passage in 2014.

The remainder of this paper is organized as follows. The wave event and wave properties deduced from satellite and radiosonde observations and the scientific issues pursued by this study are illustrated in section 2. Section 3 contains a description of the model configuration and an overview of the synoptic condition during this wave event. The simulated wave characteristics, including their spatial and temporal variations, wave spectra and wave momentum fluxes are analyzed in section 4. Wave dynamics is further examined in section 5 through ray-tracing calculations. The results and concluding remarks are included in section 6.

2. The 8-10 August 2010 wave event

The Atmospheric Infrared Sounder (AIRS) instrument (Aumann et al., 2003) on NASA's Aqua satellite is unique in its sensitivity to wave-like temperature anomalies at horizontal resolutions sufficient to resolve waves with horizontal wavelengths longer than 40 km (Alexander and Barnet, 2007). Shown in Fig. 1 are the brightness temperature patterns derived from AIRS data at several pressure levels for 8-9 August 2010. Linear wave patterns are evident over the southern tip of the Andes and Drake Passage with at least three pairs of wave crests and troughs discernible. These waves share the following properties: a) they extend across the Drake Passage with phase lines oriented northwest-southeasterly; b) while the wave crests (troughs) vary in length at different levels, their northern edges are always anchored at the southern Andes; c) the horizontal wavelengths

(i.e., the horizontal distance between two adjacent crests or troughs in the directional normal to the wave patterns) exhibit a weak dependence on the altitude, tend to increase with the distance from their northern edges, and are in the range of 300-700 km, and d) these waves are nearly stationary and penetrate throughout the lower-middle stratosphere. Further inspection indicates that the northwestern end of the wave patterns is approximately located above the Patagonian Ice Sheet, which comprises several mountain peaks higher than 3 km above the mean sea level (ASL, e.g., the highest peak, Monte San Valentin, 4058 m, and Cerro Arenales, 3437 m). The coincidence between the northwestern end of the wave patterns and these high peaks, as well as the nearly-stationary nature of these waves suggests an orographic origin.

The wind profiles derived from the radiosondes launched from Puerto Mont (PM) and Punta Arenas (PA) during this time period provide further evidence of an orographic origin of these waves (Fig. 2). Around 1200 UTC 9 August, moderate southwesterlies are directed toward the southern Andes, a condition typically conducive to the generation of strong mountain waves. Wave-like variations in the horizontal wind profiles suggest that these radiosondes may have ascended through gravity waves that emanated from the southern Andes (Fig. 3). For example, at PA, both the u and v components reveal a wave-like variation between 3 km and the tropopause (~12 km), suggesting a possible gravity wave with a vertical wavelength of ~9 km. The vertical wave length is slightly shorter (~ 7 km) at PM, consistent with weaker zonal winds around the mountaintop level (note: vertical wavelength of a hydrostatic wave is given by $2\pi U/N$, where U is the cross-mountain windspeed and N is the buoyancy frequency).

More wave properties can be deduced from the corresponding hodographs (Fig. 2b) by assuming that these wave-like perturbations were related to a monochromatic wave and using a linear dispersion relation for inertia-gravity waves (IGW). The hodographs derived from the pair of soundings are characterized by looping (or spiral) patterns which are typical for observations obtained from radiosondes ascending through gravity waves (e.g., Tsuda et al. 1994; Eckermann 1996). The radiosonde from PA experiences a much stronger wave with *u* and *v* perturbations ranging around 25-30 m s^{-1} in the troposphere (i.e., the primary loop). The counter-clockwise rotation of the loop concurrent with an increase with height implies that waves have a downward phase speed or an upward group velocity (e.g., Tsuda et al. 1994). The orientation of the primary loop implies that the horizontal wave phase line is oriented northwest-southeastward above PA. The smaller-amplitude wave observed at PM propagates upward as well. However, the major axis of the ellipsis implies that the horizontal wave vector points northwestward (Fig. 2).

Finally, it is noteworthy that this wave event is chosen through visual inspection of all the AIRS images of brightness temperature for the July-September 2010 period. Similar wave patterns are frequently observed on the AIRS images for this three-month period, implying that such waves occur frequently and may have significant contribution to the wave variance maximum over the Drake Passage, as suggested by previous studies (e.g., Jiang et al. 2002). These persistent wave patterns raise a number of scientific questions regarding their tropospheric sources, wave properties, momentum flux transfer, and interaction between these waves and stratospheric westerlies, which are addressed in the sections 3 and 4.

3. Numerical Configuration

a) Numerical set-up

The atmospheric component of the Coupled Ocean/Atmospheric Mesoscale Prediction System (COAMPS®[1], Hodur 1997; Doyle et al. 2000) had been applied to the study area (Fig. 3) to simulate this wave event. COAMPS is a fully compressible, nonhydrostatic terrain-following mesoscale model. The finite difference schemes are of second-order accuracy in time and space in this application. The boundary layer and free-atmospheric turbulent mixing and diffusion are represented using a prognostic equation for the turbulence kinetic energy (TKE) budget (Mellor and Yamada 1974). The surface heat and momentum fluxes are computed following the Louis (1979) and Louis et al. (1982) formulation. The grid-scale evolution of moist processes is explicitly predicted from budget equations for cloud water, cloud ice, rain water, snowflakes, and water vapor (Rutledge and Hobbs 1983) and the subgrid-scale moist convective processes are parameterized using an approach following Kain and Fritsch (1993). Fu-Liou's four-stream approximation is used for the short- and long-wave radiation processes (Fu et al. 1997).

The initial fields for the model are created from multivariate optimum interpolation analysis of upper-air sounding, surface, commercial aircraft, and satellite data that are quality controlled and blended with the Navy Operational Global Analysis and Prediction System (NOGAPS) forecast fields. Lateral boundary conditions for the outermost grid mesh are derived NOGAPS forecast fields. The computational domain contains two horizontally nested grid meshes of 151 × 151 and 256 × 355 grid points, and

[1] COAMPS is a registered trademark of the Naval Research Laboratory.

the corresponding horizontal grid spacings are 45 and 15 km. There are 92 vertical levels with grid spacing increasing from 20 m at the lowest model level to 400-750 m in the upper troposphere and stratosphere. The model top is located at approximately 70 km above the mean sea level and a sponge boundary condition is applied to the top 12 km to reduce downward reflection of gravity waves. The terrain data is based on the Global Land One-km Base Elevation (GLOBE) data set and the terrain in the 15-km mesh is shown Fig. 3. The model is initialized at 0000 UTC and integrated over 48-h. The first 12-h is considered as spin-up period and only the output from the 12-48 h period is used in the following diagnosis.

b) Synoptic condition overviews

The synoptic conditions associated with this wave event are illustrated in Fig. 4. During this event, the lower troposphere is characterized by complex synoptic patterns, including pressure troughs and cut-off lows associated with baroclinic waves (Figs. 4a-b). A southwesterly jet arrives at the southern Andes at 1200 UTC 8 August and reaches its maximum strength approximately 24 h later, during which the low-level winds gradually become more westerly. It is noteworthy that, according to linear theory and field observations, strong cross-mountain low-level winds are in favor of launching large-amplitude mountain waves (e.g., Doyle et al. 2009). This jet, characterized by general positive vertical wind shear, extends throughout the troposphere and provides a favorable condition for mountain waves to enter the stratosphere (Figs. 4c-d). To the north of 30^0 S, a weaker low-level jet impinges on the high central Andes ridge (~ 6 km ASL), which becomes progressively stronger during the study period. A more pronounced subtropical westerly jet is located aloft, implying that central Andes might be another wave source.

Between these two jets, the tropospheric winds are weak, associated with the approaching of a cut-off low pressure from the west of the Andes ridge.

In the stratosphere, nearly steady westerlies are evident between 50 and 70^0S parallels associated with the polar vortex. Pronounced negative meridional shear of the zonal wind (i.e., $\partial U / \partial y < 0$) exists between 40^0 and 60^0S. In contrast, the stratospheric winds to the north of 30^0S are virtually calm. The southern tip of the Andes, a possible mountain wave source, is located beneath the northern edge of the polar vortex, where relatively strong westerlies and lateral shear are present. It is worth mentioning that the simulated strong southwesterly jet extending from the mountaintop level (i.e., ~ 2 km) to the lower stratosphere over the southern Andes is consistent with radiosonde observations at PM (Fig. 2).

4. Characteristics of simulated waves

The objective of this section is to characterize the simulated gravity waves with emphasis on spatial and temporal variations of IGW and vertical wave momentum transfer. We use the simulation results from the 15-km grid, which covers the area of interest (i.e., southern Andes, Drake Passage, and a portion of the Antarctic Peninsula) and also has a horizontal grid spacing that is fine enough to resolve the mesoscale waves of interest (i.e., a few hundreds of kilometers of horizontal wavelengths).

a) Wave characteristics and time dependence

We begin with a qualitative comparison between the simulated wave patterns evident in the plan-views of the vertical velocity and those in the AIRS images in Fig. 1. Figures 5b-d approximately correspond to the pressure levels of 80, 10 and 2.5 hPa, respectively. The simulated vertical velocity field is characterized by quasi-linear wave

patterns in the stratosphere and mesosphere, oriented northwest-southeasterly across the Drake Passage in a manner qualitatively similar to the AIRS brightness temperature patterns (Fig. 1). The zonal wavelengths (i.e., east-west distance between two adjacent wave crests or toughs) exhibit some variations in the vertical and meridional directions and are in the range of 300-700 km, in agreement with those estimated from the AIRS images. The northern edges of these linear wave patterns are anchored over the southern tip of the Andes as well. The qualitative agreement between the satellite observations and COAMPS simulated wave patterns provides the basis for further diagnosis of the wave properties and exploration of the underlying dynamics.

According to COAMPS, the amplitude of the stratospheric-mesospheric wave patterns across Drake Passage generally increases with the altitude. However, in the troposphere, there are only quasi-stationary waves locally over the leeside of the central and southern Andes, and no discernible waves over the Drake Passage (Fig. 5a). The vertical variation of the simulated waves is more evident in Fig. 6 which shows vertical cross-sections of u, w, and potential temperature, θ, along three west-east sections oriented across the central and southern Andes and Drake Passage, respectively (i.e., approximately along the prevailing wind direction). Mountain waves emanate from the high central Andes ridge and propagate up to the tropopause (~12 km ASL). The zonal winds are characterized by a strong backward shear across the tropopause and lower stratosphere, and become virtually calm in the stratosphere, where no wave patterns are distinguishable (Figs. 6a-b). In contrast, deep westerlies are present over the southern Andes (Fig. 6c). Accordingly, the mountain waves that emanate from the southern Andes (i.e., Patagonian Glacial Sheet) propagate throughout the stratosphere with increasing

wave amplitude aloft, likely due to the decrease of the air density (Fig. 6d). The wave amplitudes in terms of vertical velocity and zonal wind perturbation reach maxima between 50 and 60 km ASL, where a zonal wind reversal occurs in accordance with the wave-induced steepened isentropes (Fig. 6c), a typical signature of breaking gravity waves. A useful index for diagnosing wave saturation or breaking is $\Lambda = N\eta_m / U$ (Lindzen 1981), where N is the buoyancy frequency, U is the ambient horizontal wind speed, and η_m denotes the maximum vertical displacement of density surfaces or isentropes. Wave breaking may occur when Λ exceeds unity, and accordingly keeps the maximum Λ near or less than unity. For a stationary two-dimensional wave of the form $(w,\eta) = (w_m, \eta_m)\sin(2\pi x / \lambda_x)$, the wave-induced vertical displacement can be estimated using the linear wave relation, $w = U\partial\eta / \partial x$, which yields, $\Lambda = N\lambda_x w_m / (2\pi U^2)$. Using values estimated from Fig 6c at the level of 50 km ASL, namely, N = 0.02 s^{-1}, λ_x = 300 km, w_m = 5 m s^{-1}, and U = 70 m s^{-1}, we obtain Λ ~ 1.0, implying that wave breaking may occur around 50 km ASL over the southern Andes. Along the Drake Passage, gravity waves are evident in the stratosphere and, again, there is no discernible wave signal in the troposphere (Figs. 6e-f). Compared to waves over Patagonia, the waves over the Drake Passage are characterized by smaller amplitudes and longer wavelengths. There is no sign of wave breaking, which is consistent with the stronger zonal winds and smaller vertical displacement of isentropes (therefore, A is much less than unity).

During the 36-h study period, the simulated waves evolve with time in accordance with the slowly-changing synoptic conditions. Right above the Patagonian peaks, a nearly-stationary wave is present over the leeslope characterized by a crest and trough

pair and the wave amplitude becomes much stronger over the last 24-h of the simulation (Fig. 7a), consistent with the enhancement of the cross-mountain wind component at the mountaintop level near Patagonia during the same time period (Fig. 4). In the stratosphere, there are three crest-trough pairs over the leeside of the Patagonian peaks (Fig. 7b) likely due to dispersion of the IGWs, and the characteristic wavelength is noticeably longer than in the troposphere. In contrast to the steady waves at the mountaintop level, the wave amplitude and the location of the wave phase lines slowly oscillates, namely, moving upstream first and downstream in the last 24-h. The evolution of the zonal wind component upstream of the Patagonia from the troposphere to lower mesosphere and the corresponding lee-side wave response are shown in Figs. 7c and d. The zonal wind component in the troposphere exhibits a minimum approximately from 10 to 20 h, separating the 36-h period into a weakening phase (i.e., 0-12 h) and strengthening phase (~12-24 h, Fig. 7c). The wave phase lines of these descend over more than 5 km in the first 12 h while the wave amplitude weakens substantially, and then ascend throughout the remainder of the forecast period, while the waves intensify (Fig. 7d), approximately in phase with evolution of the tropospheric westerlies. The downward and upstream (upward and downstream) movement of the phase lines during the weakening (strengthening) phase of the synoptic scale westerlies in the x-z space is consistent with the idealized study of Chen et al. (2005). The evolution of the simulated wave characteristics and the underlying dynamics are further examined in section 5 using a ray-tracing approach.

b) Wave momentum fluxes

A key property of gravity waves is the vertical flux of the horizontal momentum, defined by

$$(\bar{F}_x, \bar{F}_y) = \bar{\rho}_a(\overline{w'u'}, \overline{w'v'}) = \bar{\rho}_a \iint_A (w'u', w'v')dxdy / A, \qquad (1)$$

where $(u', v', w') = (u - U, v - V, w - W)$ denotes the perturbation velocity with respect to the synoptic-scale velocity, (U, V, W) and $\bar{\rho}_a = \bar{\rho}_a(z)$ is the mean air density which decays exponentially with the altitude, *z*. The synoptic-scale velocity at each model grid point is obtained by applying a moving average over a square area centered at this point with an area of 900 × 900 km^2. It is noteworthy that the choice of this area is largely based on trial and error, and is consistent with the traditional assumption that the characteristic wavelengths of gravity waves are usually far less than 1000 km and the length scales for synoptic patterns are typically longer than 1000 km. The calculation has been repeated with the average square area equal to 600 × 600 km^2 and 1200 × 1200 km^2, and the resulting synoptic and perturbation fields are qualitatively similar.

For a steady vertical propagating wave, the vertical momentum flux should be constant with height (Eliassen and Palm 1961) to a level where dissipation (i.e., wave breaking or critical level absorption) occurs and the wave momentum flux is deposited into the mean flow. The evolution and vertical variation of the domain-average $\bar{F}_x$ is shown in Fig. 8. It is evident that $\bar{F}_x$ is negative, as expected of typical upward propagating mountain waves. The amplitude of $\bar{F}_x$ exhibits a sharp decrease between approximately 15 and 20 km ASL, likely associated with the backward vertical wind shear (Fig. 6a). In the stratosphere and lower mesosphere, the amplitude of $\bar{F}_x$ decreases gradually with the altitude. The momentum flux also shows two separate maxima in time

in the stratosphere, corresponding to the first 12 h and last 24 h, respectively, which is consistent with the evolution of the stratospheric waves in Fig. 7. In order to examine the meridional variation of the wave momentum flux, the zonally-averaged vertical flux of the zonal momentum, $< F_x >= \bar{\rho}_a \overline{w'u'} = \bar{\rho}_a \int_0^L w'u' dx / L$, where L is the zonal width of the 15-km model grid, for the final hour of the simulation is shown in Fig. 9. The simulated tropospheric momentum fluxes are characterized by three local maxima in amplitude over the high ridge of central Andes, the Patagonian peaks in the southern Andes, and the Antarctic Peninsula, respectively. The amplitude of the maxima over central Andes and Patagonia decay monotonically with the altitude, implying their orographic origins. The maximum over the Patagonian peaks is substantially stronger than the one over the high central Andes ridge, likely due to stronger zonal winds over Patagonia in the lower troposphere. The maximum over Antarctic Peninsula is centered approximately at 8 km ASL, pointing to baroclinic wave adjustment as a possible source.

A substantial portion of the wave momentum flux that originates from the Patagonian peaks extends well into the stratosphere and even lower mesosphere. In contrast, the momentum flux from the central Andes is mostly absorbed in the upper troposphere and lower stratosphere, on account of the backward vertical shear of zonal winds. It is also noteworthy that the momentum flux over the Antarctica Peninsula reduces to virtually zero around 10 km ASL. Interestingly, in the stratosphere, the momentum flux maximum over Patagonia splits into two separate maxima with the primary one extending vertically upwards and the second with a comparable amplitude tilting southward over the Drake Passage, indicative of a southward transfer of the wave

momentum flux. At 60-km ASL, the center of the second maximum is located approximately 1000 km to the south of Patagonia.

To further examine the dependence of the momentum flux on horizontal wave numbers, the momentum flux in the wave number space is computed for a 256 x 256 sub-domain of the 15-km grid, which includes the southern Andes and Drake Passage (Fig. 5d). The momentum flux is analyzed using a double Fast Fourier Transform technique. Figure 10 displays the vertical fluxes of the zonal momentum in the horizontal wave number space, defined by (e.g., Eckermann et al. 2010)

$$\hat{F}_x(k,l) = \frac{\bar{\rho}}{4}(\hat{u}\hat{w}^* + \hat{u}^*\hat{w}) \qquad (2)$$

where the over-hat denotes Fourier transformed variables (i.e., u, w, and F_x) and the terms with the asterisk represent the corresponding conjugates. The momentum flux spectrum in the troposphere is characterized by positive and negative maxima over relatively small wave numbers. There are two negative maxima centered around ($6k_m$, $4k_m$) and ($4k_m$, $-2k_m$), corresponding to the waves with northwest-southeast and southwest-northeast oriented phase lines, respectively. In addition, there is a positive maximum near (0, $2k_m$), a plausible source of which is the projection of mesoscale waves onto synoptic flow variations. As shown in Fig. 4, synoptic flow patterns are rather complicated in the troposphere, implying difficulty in separating mesoscale wave perturbations and synoptic scale variations. The contribution to momentum fluxes from the synoptic-scale variability can be either positive or negative. It has been demonstrated by Chen et al. (2005) that positive momentum flux can be generated by interaction between mountain waves and evolving large-scale patterns. It is noteworthy that in the troposphere, even the negative momentum flux maxima may be contaminated by contributions from synoptic-scale flow

patterns. This is much less an issue in the stratosphere where momentum fluxes are predominantly negative (Fig. 10b-d). In addition, the negative maxima are centered above l=0, implying that the southwest-northeast oriented waves evident in the troposphere are absent in the mid-stratosphere, likely due to critical level absorption associated with the vertical wind shear in the tropopause and lower stratosphere. This is consistent with the wave patterns in Fig. 4, phase lines of which are mostly northwest-southeast oriented. At 20 km ASL, the momentum flux maximum is centered approximately at ($6k_m$, $6k_m$), corresponding to wavelengths (640 km, 640 km). From the lower to middle stratosphere, the momentum flux maximum tends to shift slightly toward larger wave numbers. For example, at 45 km ASL, the maximum is centered near ($8k_m$, $9k_m$), corresponding to wavelengths of (480 km, 426 km). The shortening of the horizontal wavelengths aloft may result from the difference in the vertical group velocity; in general, shorter waves propagate faster (e.g., Chen et al. 2005). The amplitude of the momentum flux tends to slowly decrease with the altitude and a sharp decrease occurs between 45 and 55 km (Figs. 10c-d), likely associated with wave breaking over Patagonia.

5. Ray-tracing calculation

The analysis in section 4 suggests that the observed stratospheric/mesospheric wave patterns over Drake Passage likely originate from the Patagonian peaks in the southern Andes. It also raises a number of interesting questions regarding the influence of lateral and vertical wind shear, stratification variation, and the earth's rotation on wave propagation, refraction, evolution and possible absorption. In this section, we attempt to address these questions through three-dimensional ray-tracing calculations using the COAMPS output from the 15-km grid.

a) Three-dimensional ray paths of inertial gravity waves

The ray-tracing technique has been frequently used in the study of stratospheric waves (e.g., Dunkerton 1983; Sato et al. 2009). A ray trajectory is given by (Lighthill 1978)

$$\frac{d_g x_i}{dt} = U_i + c_{gi}, \tag{3}$$

where $\frac{d_g}{dt} = \frac{\partial}{\partial t} + (\vec{U} + \vec{c}_g) \bullet \nabla$ denotes changes along a ray path and $c_{gi} = \partial\omega / \partial k_i$ is the intrinsic group velocity and the index i=1, 2, and 3, corresponding to the three dimensions, x, y, and z. Using the Wentzel-Kramers-Brillouin (WKB) approximation, the dispersion relation for a linear hydrostatic IGW can be written as

$$\omega^2 = \frac{N^2 K^2}{m^2} + f^2 \tag{4}$$

where $N^2 = \frac{g}{\bar{\theta}} \frac{\partial \bar{\theta}}{\partial z}$ is the buoyancy frequency squared, $K^2 = k^2 + l^2$ is the total horizontal wave number squared, k and l are horizontal wave numbers, m is the vertical wave number, f is the Coriolis parameter, $\omega = \Omega - \vec{k} \bullet \vec{U}$ is the intrinsic frequency, and Ω is the Eulerian wave frequency. The density scale height effect is ignored in (4), as our focus is on hydrostatic waves. The group velocity ($\vec{c}_g$) can be written as

$$\vec{c}_g = \frac{N^2}{\omega m^2} \left[k, l, -K^2 / m \right] \tag{5}$$

Using $\frac{dk_i}{dt} = -\frac{\partial \omega}{\partial x_i}$ and Eqn. (4), we obtain the equations that govern refraction of a wave vector (e.g., Dunkerton 1984; Edwards and Staquet 2005):

$$\frac{d_g k}{dt} = -k \frac{\partial U}{\partial x} - l \frac{\partial V}{\partial x} - \frac{K^2}{2m^2} \frac{\partial N^2}{\partial x} \tag{6}$$

$$\frac{d_g l}{dt} = -k\frac{\partial U}{\partial y} - l\frac{\partial V}{\partial y} - \frac{K^2}{2m^2}\frac{\partial N^2}{\partial y} - \frac{f}{\omega}\frac{df}{dy} \tag{7}$$

$$\frac{d_g m}{dt} = -k\frac{\partial U}{\partial z} - l\frac{\partial V}{\partial z} - \frac{K^2}{2m^2}\frac{\partial N^2}{\partial z}. \tag{8}$$

Equations (6-8) imply wave refraction occurs associated with lateral and vertical wind shears, horizontal and vertical stratification gradients and β-effect. In the remainder of this section, several groups of inertia-gravity wave ray paths and refraction are calculated using (3) and (6-7) with the wind and buoyancy frequency fields derived from the COAMPS simulation. The objective of these calculations is to understand the vertical and lateral propagation of IGWs, the influence of lateral wind shear and the earth's rotation effects on IGW propagation, and the evolution of IGWs in a time-evolving synoptic flow. The integration of a ray terminates under one of the following five conditions: a) when it reaches lateral boundaries or the model top; b) when the nondimensional parameters, $\delta_i = \frac{1}{k_i^2}\left|\frac{dk_i}{dx_i}\right| > 1$; c) when ω changes sign; d) when ω^2-f^2 <0; and e) when m is too large. Condition b) states that the variation of wave numbers should be slow, which is required by the WKB approximation (Marks and Eckermann 1994; Chen et al. 2005). The sign change of ω implies that the ray is traveling across a critical level. When condition d) is satisfied, the inertial-gravity wave becomes evanescent, or "trapped". When m is too large, the vertical group velocity is small, implying that the ray is approaching a critical level. It is noteworthy that Eqn. (8) is redundant with the dispersion relation (4). In our code, the vertical wave numbers are calculated using (4) and (8) separately for the purpose of consistency checking.

b) Ray paths in steady state flow

To examine the latitudinal dependence of wave characteristics, we first calculate rays initiated from a range of latitudes along the main Andes ridge using winds and potential temperature averaged over the last 24-h of the integration. The 24-h averaged fields are further smoothed to remove mesoscale perturbations, which may introduce strong wind shear and cause problems in the integration. This is done using the same two-dimensional 900 x 900 km^2 smoother as in the wave momentum flux calculation. Furthermore, the model wind direction at each grid point is rotated from the model north to the true north to remove errors associated with the map projection. The smoothed and corrected zonal winds are characterized by a stratospheric jet core approximately at 50 km ASL (Fig. 11b). To the south of 30^0 S, there is a positive vertical shear (i.e., $dU/dz>0$) and negative lateral shear (i.e., $dU/dy<0$).

These rays are initiated approximately along the main southern Andes ridge (Fig. 12) and from 6 km ASL to further minimize the impact of mountain induced mesoscale perturbations. The initial horizontal wave numbers are $k_0 = l_0 = 2\pi/400$ km^{-1}, which are chosen based on the spectral analysis in section 4. As shown in Fig. 12, these ray paths behave quite differently, dependent on their initial latitudinal locations. For rays initiated over the high central Andes ridge to the north of 35^0S, the vertical group velocity decreases toward zero between 15 and 20 km, in accordance to the backward vertical shear of the westerly winds above the tropopause (Fig. 11b), suggestive of critical level absorption. Although the wave packets launched between 35^0 and 40^0 S are able to avoid the critical level, partially attributed to their southward propagation, they reach the eastern model boundary first instead of entering into the polar jet. These waves are of less interest because of the slow zonal wind in the lower troposphere and the relatively low

quasi-two-dimensional ridge between 30-40^0 S. The rays initiated between 40^0 and 52^0 S experience the largest southward tilting (i.e., 500-1200 km) and are able to propagate into the stratosphere jet core. It is noteworthy that, above the zonal jet, the group velocity decreases associated with the backward vertical shear of the zonal wind, which should eventually lead to wave breaking. The southward bending of the ray paths that originate from the high Patagonian peaks is consistent with the bifurcation of the vertical flux of the zonal momentum in Fig. 9b, and suggests that the Patagonian peaks are probably the source of the impressive stratospheric/mesospheric waves over Drake Passage revealed by the AIRS brightness temperature images. Between 52^0 and 62^0 S, the waves propagate nearly vertically with much less lateral refraction. There is no high terrain within this latitudinal range and accordingly, mountain waves from this area have little contribution to the simulated stratospheric waves aloft. Further south, no rays are shown as the intrinsic frequency changes signs near the surface due to the complex tropospheric wind patterns (Figs. 4a-b), implying a flow condition unfavorable for mountain wave generation.

As an example, a group of ray paths corresponding to $k_0 = 2\pi/400$ km^{-1} and $l_0 = 0$ are calculated and included in Fig. 12. These rays bifurcate approximately at 47^{0}S, just to the north of Patagonia. To the north of 47^{0}S, the rays bend northward in the troposphere due to the positive meridional wind component and absorbed by the critical level aloft. To the south, the rays bend southward associated with the negative meridional wind and the increase of l (i.e., positive l and accordingly negative meridional group velocity) aloft. In general, this group of rays show less southward bending than the corresponding rays with $k_0 = l_0$. For example, at 45 km ASL, the wave packets with $k_0 = 2\pi/400$ km^{-1} and $l_0 =$

0 launched from Patagonia are approximately located at 150 km to the south of the wave source. More ray paths over a range of wave numbers from Patagonia are shown in Fig. 13. Along each ray path, the meridional wave number increases, primarily due to the negative lateral shear of the westerlies (i.e., $\frac{\partial U}{\partial y} < 0$) and the zonal wave number becomes slightly smaller. In general, shorter waves (i.e., $\lambda_x < 300$ km) propagate faster in the vertical with little southward bending. This is especially true for the packets with $l_0 = 0$, the ray paths of which are nearly vertical. Longer waves (i.e., λ_x =400 and 600 km) propagate slower upward, and therefore, reach further south in the stratosphere and mesosphere. It is noteworthy that, even for l_0 =0, the rays of longer waves (i.e., λ_x~ 600 km or longer) exhibit substantially more southward refraction associated with the increase of the meridional wave number along each ray and slower vertical group velocity. In summary, the ray path calculation suggests that the northwest-southeast oriented wave patterns over Drake Passage are likely one branch of the three-dimensional waves from Patagonia (Smith 1980) while the other branch is largely absorbed by critical levels to the north of Patagonia. The southward transfer of wave momentum flux is enhanced by wave refraction associated with the strong lateral shear of zonal winds aloft. The stratospheric momentum flux maximum right above the Patagonian peaks is associated with waves relatively short waves (i.e., $\lambda_x \sim 300$ km or shorter). The wavelength dependence of the southward ray bending is consistent with the observed and simulated increase of wave lengths aloft with distance away from the wave source (i.e., Patagonia).

Finally, we briefly discuss the sensitivity of the ray path corresponding to $k_0 = l_0 = 2\pi/400$ km^{-1} generated by flow over Patagonia to the Coriolis parameter, buoyancy frequency, vertical wind shear and meridional winds. Although the spatial variation of the buoyancy frequency and Coriolis parameter appear in Eqns. (3-8), their impact on wave refraction is rather insignificant over the parameters examined here (Fig. 14). This is consistent with Dunkerton (1984), who calculated ray paths of IGWs with an analytical zonal jet profile similar to the mean profile shown in Fig. 11b. According to Eqn. (3), the squared ratio of the Coriolis parameter and the wave intrinsic frequency, f^2 / ω^2, provides a useful measure of the importance of the Coriolis parameter in wave refraction. We can define a wave Rossby number squared, $R_w^2 = \omega^2 / f^2$, which reduces to $R_w^2 = (Uk)^2 / f^2$ after ignoring the meridional wind. As an example, for $f = 1.2 \times 10^{-4}$ s^{-1}, U = 30 m s^{-1} and $k = 2\pi/400$ km^{-1}, we have $R_w^2 \sim 16 >> 1$, implying that the Coriolis parameter effect is negligible. It is noteworthy that the Coriolis parameter becomes important when $(Uk+lV)^2$ and f^2 are comparable. This could happen for longer waves or or Uk and lV are comparable but of opposite signs. One such example is a wave excited by northwesterly winds over Patagonia (i.e., $k, l>0$, U>0, and V<0). Another example is northward propagating waves originating from Antarctic Peninsula associated with a southwesterly jet (i.e., $k>0$, $l<0$, $U>0$, and $V>0$). When replacing the local buoyancy frequency with a constant, 0.015 s^{-1}, the ray path exhibits noticeably less refraction due to the faster upward propagation in the troposphere. It is instructive to compare the terms corresponding to the meridional wind shear and the meridional N^2 variation in Eqn. (6); the former is substantially larger than the latter. Accordingly, the horizontal variation of the N^2 is found to have little impact on wave refraction. The lateral shear of the zonal

wind (i.e., U_y) aloft plays a key role in increasing the meridional wave number along a given ray path and therefore enhancing the southward wave fraction. The difference in the meridional locations at 60 km ASL for the wave packets with the modeled V and with V =0 is small, because V is positive in the troposphere (i.e., southwesterlies) and negative in the stratosphere; the contributions from the two effects partially cancel.

c) Rays in evolving synoptic flows

It is evident that both the large-scale flow and gravity waves evolve with time during the integration on timescales of the order of 12 h, which is comparable to the time it takes for gravity waves to propagate from the ground surface to mesosphere (i.e., 6-12 h according to Figs. 12-14). To understand the wave response to the evolving large-scale flow condition, we repeat the above ray calculations using the hourly COAMPS output. Again, the hourly wind and potential temperature fields are smoothed to remove mesoscale perturbations and the wind directions are rotated relative to the true north. The winds and buoyancy frequency along a ray path are obtained by bi-linear interpolation using data at the adjacent points in both time and space. As an example, the ray paths of two wave packets initiated at 6 km ASL over Patagonian are calculated. The horizontal wave numbers are $k_0 = 2\pi/400$ km^{-1} and $l_0 = 0$, and $k_0 = l_0 = 2\pi/400$ km^{-1}, corresponding to the southeast-propagating and localized wave families, respectively (Fig. 15). It is evident that the ray characteristics vary substantially with the initiation time. A few aspects of the temporal evolution of the two sets of ray paths are worth mentioning. Firstly, there is a general correspondence between the intensity of the tropospheric westerlies and the vertical group velocity (i.e., proportional to the height difference between two adjacent dots along each ray) of the waves. For both the localized and southeast wave families, the

vertical propagation of these waves becomes increasingly faster between 1200 UTC of 8 and 9 August 2010, and accordingly, the ray paths tend to converge. The convergence is more evident for the localized wave packets, implying that a faster wave packet may be able to catch up with a slower one initiated at earlier time and accordingly wave action tends to accumulate during this flow acceleration period (Chen et al. 2005). Secondly, the wave packets slow down consistently between 10 and 15 km ASL, associated with the vertical wind shear across the tropopause, and accelerate aloft in accordance to the increase of zonal wind speed in the stratosphere. Furthermore, the meridional distance between the initial and end (i.e., ~ 60 km ASL) points of the rays increases with time for wave packets initiated between 2000 UTC 8 and 1000 UTC 9 August, partially due to the weakening of the southerly wind component with time in the troposphere.

6. Discussion and conclusions

A gravity wave event characterized by long linear wave patterns oriented northwest-southeastward across the Drake Passage in the stratosphere and lower mesosphere is examined using a COAMPS simulation, and the simulated wave patterns bear close resemblance to those revealed by the AIRS brightness temperature images.

According to the numerical simulation, the linear stratospheric wave patterns over Drake Passage likely originate from interaction between Patagonian and a southwesterly tropospheric jet. Waves from the three-dimensional Patagonian peaks can be separated into three families, namely, the northeast-propagating (i.e., $k>0$ and $l<0$), localized ($k>0$ and $l\sim0$), and southeast-propagating families (i.e., $k>0$ and $l>0$). For the northeast propagating waves, their ray paths tend to tilt northward, and accordingly these waves are eventually absorbed at the critical level between 15 and 20 km as those waves launched

from the central Andes. The localized family including relatively short waves (λ_x < 300 km and l_0 ~ 0) propagates nearly vertically and contributes to a wave momentum maximum directly over Patagonian. For this wave family, the increase of the wave amplitude with the altitude eventually leads to wave breakdown between 50-60 km ASL where the wave saturation criterion (i.e., $\Lambda = N\eta_m / U \sim 1$) is met. The southeast-propagating family incudes longer waves (i.e., λ_x > 400 km) with a small or positive meridional wave number, l_0, and transfers wave momentum flux polarward while propagating up into the stratosphere and mesosphere. The polarward propagation assisted by refraction associated with the negative lateral shear of the westerlies allows these waves to enter into the polar vortex jet in the stratosphere without suffering from wave breaking. They eventually should break down above the jet core where the zonal wind decreases aloft (i.e., 60 km ASL or higher for this case) with momentum deposited into the stratosphere or mesosphere near 60^0 S.

The southward bending of the wave rays initiated from Patagonia is found to be sensitive to both the wave characteristics and synoptic scale winds. In general, longer waves exhibit more southward refraction, largely due to their slower vertical propagation. This is consistent with the modeled and AIRS-observed wave patterns over Drake Passage, which show clear increase of the horizontal wavelengths with the distance from the southern Andes. In addition, the southward wave propagation is also dependent on the meridional wind component; a northerly component (i.e., V<0) enhances the polarward propagation. For this event, however, the contributions from the southerlies in the troposphere and northerlies in the stratosphere largely cancel each other out. Furthermore, the wave refraction is relatively insensitive to the Coriolis parameter and

the inhomogeneity in stratification. Clearly, the term corresponding to the horizontal variation of the stratification in Eqns. 5.4-5.6 is much smaller than the horizontal shear terms. For most waves examined in this study, the wave Rossby number squared, $R_w^2 = (Uk / f)^2$, is large, and accordingly, the Coriolis parameter has little impact on the wave refraction.

It is noteworthy that, compared to the waves observed over major mid-latitude barriers such as the European Alps (Smith et al. 2007) and the Sierra Nevada ridge in US (Smith et al. 2008; Doyle 2009), the *w* amplitude for the tropospheric waves over Andes is much weaker. The spectacular linear waves over the Drake Passage in the stratosphere and mesosphere largely result from the growth of the wave amplitude with the altitude due to the approximately exponential decrease of the air density aloft. The Patagonian high peaks are located under the northern edge of the deep intense westerly jet associated with the relatively steady polar vortex. Accordingly, waves from Patagonia are able to propagate into stratosphere and mesosphere without significant amplitude reduction from critical level absorption or wave breaking; the latter often occurs associated with backward wind shear (e.g., above the polar vortex jet core in this case). In contrast, waves over low- to mid-latitude barriers typically encounter some form of critical levels in the upper troposphere to lower stratosphere (e.g., a critical level at ~ 21 km was found over the Sierra Nevada Range during T-REX; waves over the Central Andes are absorbed by a critical level between 15-20 km ASL in this study). These results highlight the importance of high latitude topography such as the southern Andes, Antarctic Peninsula, and Greenland in stratospheric/mesospheric drag parameterization. In a recent study, McLandress et al. (2012) suggested that the missing orographic wave drag near 60^0S

likely be the cause of the stratospheric wind biases in global models. This study suggests that orographic wave drag near 60^0S may have a nonlocal source, the Patagonian peaks, and the wave momentum flux is transferred southward by southeast-propagating IGWs. The lateral shear of the horizontal wind along the edge of the polar vortex plays a constructive role in the southward momentum transfer largely through increasing the meridional wave number. As the dominant refraction term in (7), $-k\frac{\partial U}{\partial y}$, needs time to act, the longer waves with slower vertical group velocity stay in the shearing region long enough to be refracted. In general, the above results are consistent with the ray path calculations by Sato et al. (2009) using global model data. Clearly, further studies are needed to quantify and evaluate the climatological aspects of the orographic drag maximum over Drake Passage, such as the occurrence frequency, temporal evolution and mean amplitudes, so that these waves and associated momentum fluxes can be properly represented in global and climate models.

Finally, while the wave characteristics and the ray-tracing calculations are consistent with waves emanated from Patagonia, we cannot rule out other wave sources, such as the jet-stream or frontal excitation, which may have contributed to the momentum fluxes. This study provides some useful guidance for planning future field observations of gravity waves over the southern Andes and Drake Passage. For example, according to our results, it is difficult for research aircraft to sample orographic waves over Drake Passage using airborne *in-situ* instruments. On the other hand, upward-looking remote sensing instruments on research aircraft flying along the Drake Passage may provide much needed insight into the characteristics and dynamics these stratosphere-mesosphere waves.

Acknowledgements.

This research is supported by the NRL Base Program. The simulations were made using the Coupled Ocean/Atmospheric Mesoscale Prediction System (COAMPS) developed by US Naval Research Laboratory. Computational resources were supported by a grant of HPC time from the Department of Defense Major Shared Resource Centers.

References

Alexander, M. J. and R. A. Vincent, 2000: Gravity waves in the tropical lower stratosphere: A model study of seasonal and interannual variability. *J. Geophys. Res.*, **105**, 17983-17994.

Alexander, M. J., and C. Barnet, 2007: Using satellite observations to constrain parameterizations of gravity wave effects for global models, *J. Atmos. Sci*., **64**, 1652-1665.

Alexander, M. J., J. Gille, C. Cavanaugh, M. Coffey, C. Craig, V. Dean, T. Eden, G. Francis, C. Halvorson, and co-authors, 2008: Global estimates of gravity wave momentum flux from High Resolution Dynamics Limb Sounder observations. *J. Geophys Res.* **113**: D15S18, DOI: 10.1029/2007JD008807.

Alexander, M. J., S. D. Eckermann, D. Broutman, and J. Ma, 2009: Momentum flux estimates for South Georgia Island mountain waves in the stratosphere observed via satellite. *Geophys. Res. Lett.*, **36**, L12816, doi:10.1029/2009GL038587.

Aumann, H. H., M. T. Chahine, C. Gautier, M. D. Goldberg, E. Kalnay, L. M. McMillin, H. Revercomb, P. W. Rosenkranz, W. L. Smith, D. H. Staelin, L. L. Strow and J. Susskind, 2003: AIRS/AMSU/HSB on the Aqua mission: design, science objectives, data products and processing system, *IEEE Trans. Geosci. and Remote Sensing*, **41**, 253-264.

Carslaw, K. S., M. Wirth, A. Tsias, B. P. Luo, A. Dörnbrack, M. Leutbecher, H. Volkert, W. Renger, J. T. Bacmeister. E. Reimer and T. Peter, 1998: Increased stratospheric ozone depletion due to mountain-induced atmospheric waves. *Nature*, **391**, 675-678.

Chen, C., D. R. Durran, and G. J. Hakim, 2005: Mountain-wave momentum flux in an evolving synoptic-scale flow. *J. Atmos. Sci*., **62**, 3213-3231.

Doyle, J. D. and Coauthors, 2000: An intercomparison of model predicted wave breaking for the 11 January 1972 Boulder windstorm. *Mon. Wea. Rev.,* **128,** 901–914.

Dunkerton, J. T., 1984: Inertia-gravity waves in the stratosphere. *J. Atmos. Sci.*, **41**, 3396-3404.

Eckermann, S. D., 1996: Hodographic analysis of gravity waves: Relationships among Stokes parameters, rotary spectra and cross-spectral methods. *J. Geophys. Res*., **101**, 19169019174.

Eckermann, S. D. and co-authors, 2006: Imaging gravity waves in lower stratospheric AMSU-A radiances, Part 2: Validation case study. *Atmos. Chem. Phys*., **6**, 3343-3362.

Eckermann, S. D., J. Lindeman, D. Broutman, J. Ma, and Z. Boybeyi, 2010: Momentum fluxes of gravity waves generated by variable Froude number flow over three-dimensional obstacles. *J. Atmos. Sci.*, **67**, 2260-2278.

Eliassen, A. N. and E. Palm, 1961: On the transfer of energy in stationary mountain wave. *Geof. Pub*., **22**, 1-23.

Fritts, D. C. and M. J. Alexander, 2003: Gravity wave dynamics and effects in the middle troposphere, *Rev. Geophys*., **41**, 3-1.

Gong, J., D. L. Wu, and S. D. Eckermann, 2012: Gravity wave variances and propagation derived from AIRS radiances. *Atmos. Chem. Phys.,* **12**, 1701-1720.

Grubišić, V., J. D. Doyle, J. Kuettner, R. Dirks, S. A. Cohn, L. L. Pan, S. Mobbs, R. B. Smith, C. D. Whiteman, S. Czyzyk, S. Vosper, M. Weissmann, S. Haimov, S. F. J. De Wekker, and F. K. Chow, 2008: The Terrain-Induced Rotor Experiment A Field Campaign Overview Including Observational Highlights. *Bull. Amer. Meteor. Soc.*, **89**, 1513-1533.

Lighthill, M. J., 1978: *Waves in Fluids*, Cambridge University Press.

Lilly, D. K. and P. J. Kennedy, 1973: Observations of a stationary mountain wave and its associated momentum flux and energy dissipation. *J. Atmos. Sci*., **30**, 1135-1152.

Lindzen, R. S., 1981: Turbulence and stress due to gravity wave and tidal breakdown. *J. Geophys. Res.*, **86**, 9707-9714.

McLandress, C., T. G. Shepherd, S. Polavarapu, and S. R. Beagley, 2012: Is missing orographic gravity wave drag near 60^0S the cause of the stratospheric zonal wind biases in chemistry-climate models? *J. Atmos. Sci.*, **69**, 802-818.

Jiang, J., D. Wu, and S. D. Eckermann, 2002: Upper Atmosphere Research Satellite (UARS) MLS observation of mountain waves over the Andes. *J. Geophys. Res*., **107**: 8273, DOI: 10.1029/2002JD002091.

Kim, Y.-J., S. D. Eckermann, and H.-Y. Chun, 2003: An overview of the past, present, and future of gravity-wave drag parameterization for numerical climate and weather prediction models. *Atmos.-Ocean*, **41**, 65-98.

Moffat-Griffin, T., R. E. Hibbins, M. J. Jarvis, and S. R. Colwell, 2011: Seasonal variations of gravity waves over an Antarctic Peninsula station. *J. Geophys. Res.* **116**, D14111, doi:1029/2010JD015349.

Plougonven, R., A. Hertzog, and H. Teitelbaum, 2008: Observations and simulations of a large-amplitude mountain wave breaking over the Antarctic Peninsula. *J. Geophys. Res*. **113**, D16113, doi:10.1029/2007JD009739.

Sato, K., S. Watanabe, Y. Kawatani, Y. Tomikawa, K. Miyazaki, and M. Takahashi, 2009: On the origin of mesospheric gravity waves. Geophys. Res. Lett., 36, L19801, doi:10.1029/2009GL039908.

Shutts, G. J. and S. B. Vosper, 2011: Stratospheric gravity waves revealed in NWP model forecasts. *Q. J. R. Meteorol. Soc*., DOI:10.1002/qj.763.

Smith, R. B., 1980: Linear theory of stratified hydrostatic flow past an isolated mountain. *Tellus*, **32**, 348-364.

Smith, R. B., J. D. Doyle, Q. Jiang, and S. A. Smith, 2007: Alpine gravity waves: Lessons from MAP regarding mountain wave generation and breaking. *Q. J. R. Meteorol. Soc*., **133**, 917-936.

Smith, R. B., B. K. Woods, J. Jensen, W. A. Cooper, J. D. Doyle, Q. Jiang, and V. Grubisic, 2008: Mountain waves entering the stratosphere. *J. Atmos. Sci*., **65**, 2543-2562.

Spiga, A., H. Teotelbaum, and V. Zeitlin, 2008: Identification of the sources of inertia-gravity waves in the Andes Cordillera region. *Ann. Geophs*., **26**, 2551-2568.

Tsuda, T., Y. Murayama, H. Wiryosumarto, S. W. B. Harijono, and S. Kato, 1994: Radiosonde observations of equatorial atmosphere dynamics over Indonesia, II: Characteristics of gravity waves. J. Geo. Res., 99, 507-516.

Wu, DL. 2004: Mesoscale gravity wave variances from AMSU-A radiances. *Geophys. Res. Lett*. **31**: L12114, DOI: 10.1029/2004GL019562.

Caption:

Figure 1. Small horizontal scale brightness temperature anomalies (K) extracted from multichannel AIRS radiances peaking at the indicated altitudes of (from bottom to top) 80 hPa, 30 hPa, 7 hPa and 2.5 hPa (see Table A2 and accompanying discussion of Gong et al. 2012 for channel details) from the ascending and descending overpasses of the southern Andes region on 8 and 9 August 2010. These perturbations were isolated by fitting and then subtracting along-track radiance structure with horizontal scales >600 km, including systematic limb effects as a function of scan angle (Eckermann et al. 2006). A 3x3 point smoothing of radiance anomalies in neighboring footprints was applied in these plots to suppress channel noise and accentuate the geophysical wave perturbations.

Figure 2. Wind and potential temperature profiles from the 1200 UTC, 9 August 2010, Puerto-Montt (PM, 41.43S, 73.10W; solid) and Punta-Arenas (PA, 53.00S, 70.85W; dashed) soundings are shown in a). The corresponding hodographs are plotted in b) with the rotating direction of the primary loop for each sounding indicated by thin arrows. The bold-dashed arrows indicate plausible wave vector directions.

Figure 3. Topography in the 15-km grid domain is shown in gray shading (interval= 0.5 km). The locations of the two radiosonde stations, Puerto Mont (PM) and Punta Arenas (PA), are indicated by triangles.

Figure 4. Synoptic flow patterns from the 45-km grid. The horizontal wind speed (color, increment is 5 m s^{-1} for a-d and 10 m s^{-1} for e-f), wind vectors, and pressure contours at the 4-km, 10-km, and 35-km levels valid at 1200 UTC 8 August 2010 are shown in the left panels. The corresponding graphics for 1200 UTC 9 August 2010 are shown in the right panels. The pressure contour intervals are 5 hPa for the 4-km and 10-km levels and 0.5 hPa for the 35-km level.

Figure 5. Plan-views of the vertical velocity (color, increment is 0.2 for a-c and 0.3 m s^{-1} for d) and horizontal wind vectors at a) 4, b) 10, c) 17, and d) 30 km ASL, respectively, valid at 1200 UTC, 9 August, 2010. The three bold lines and star in a) indicate the locations of the three cross-sections shown in Fig. 6 and the location for time-height diagram in Fig. 7c, respectively.

Figure 6. Cross-sections of zonal (i.e., *u*, left, increment is 5 for a and 10 m s^{-1} for c and e) and vertical (i.e., *w*, right, increment is 0.3 for b, 1 for d and 0.5 m s^{-1} for f) wind components oriented across the Central Andes (top), Patagonian (middle), and Drake Passage (bottom, see Fig. 5a for locations) valid for 1200 UTC, 9 August 2010.

Figure 7. Shown in a) and b) are distance-time (i.e., Hovemöller) diagrams of the vertical velocity at 4 km (incr.: 0.2 m s^{-1}) and 40 km (incr.: 1 m s^{-1}) ASL along the same cross-Patagonia section as in Figs. 6c-d (but over a shorter distance). Shown in c) and d) are time-height diagrams of the upstream zonal winds (incr.: 5 m s^{-1}, see Fig. 5a for location)

and vertical velocity (incr.: 1 m s^{-1}, superimposed with the corresponding isentropes, incr.: 100 K) in the leeside.

Figure 8. Time-height plots of the vertical flux for the zonal momentum (i.e., F_x) averaged over the southern Andes and Drake Passage. For the troposphere (lower), the range is from -0.06 to 0 with an increment of 0.005 N m^{-2}, and for the stratosphere, the range is from -0.012 to 0 with an increment of 0.001 N m^{-2}.

Figure 9. Vertical cross-section of vertical fluxes of the zonal momentum for the lowest 15 km (lower) and between 15 and 60 km ASL (upper) valid at 0000 Z (a and c) and 1200 Z, 9 August 2010, respectively. The grayscale intervals are 7.5×10^3N $m^{-1}$for a) and 45×10^3N m^{-1} for b).

Figure 10. The vertical flux of zonal momentum spectra (i.e., $\hat{F}_x(k,l)$) at 12, 20, 45 and 55 km above MSL valid at 1200UTC, 9 August 2010 are shown in grayscale (intervals are 0.15, 0.08, 0.05, and 0.03 N m^{-2}) and contours (intervals=0.3, 0.16,0.1, and 0.06 N m^{-2}; negatives are dashed). The horizontal and vertical axes correspond to zonal and meridional wave numbers. Only wave numbers in the range of $1 \le k \le 23k_m$ and $-21k_m \le l \le 21k_m$ are shown, where $k_m = 2\pi/(256\Delta x)$.

Figure 11. Plan-view of the 24-h average true zone (grayscale, incr. = 10 m s^{-1}) and meridional (contour, incr. = 5 m s^{-1}, negatives are dashed) wind components at 10 km ASL is shown in a). Panel b) shows a vertical cross-section of the true zone wind

component (grayscale, incr. = 10 m s^{-1}) and isentropes (incr. = 100 K) oriented north-southly approximately along the Andes ridge (location indicated by the solid line in a).

Figure 12. Ray paths in the y-z plane calculated using the 24-h average COAMPS winds and buoyancy frequency are shown. These rays are initiated at x=105 (in grid points) and z = 6 km with $k_0 = 2\pi/400$ (km^{-1}). Two sets of ray paths are shown, he solid rays correspond to y = 20n (n=1, 2, 3…) in model grid points and $l_0 = k_0$, and the dashed rays correspond to y=20n + 10 and l_0 =0. The time interval between two adjacent symbols (i.e., circles for set 1 and crosses for set 2) is 1 hour. The maximum terrain height is shown below. The dash-bolded lines here and in Figs. 13-15 indicate the bottom level of the model sponge layer.

Figure 13. Ray paths in the y-z plane (a) and horizontal wave numbers (k, l) (b) along each ray path for four pairs of wave packets with $k_0 = 2\pi/100$, $2\pi/200$, $2\pi/400$, and $2\pi/600$ (km^{-1}) and l_0 =0 and k_0, respectively. In (b), the k (solid) and l (dashed) curve are shown in the same color as in a) for each wave packet.

Figure 14. Ray paths in the y-z plane (a) and wave numbers (b) are shown for $k_0 = l_0 = 2\pi/400$. The other five pairs of curves correspond to paths and wave numbers calculated from the identical parameters except for f=0, U_y =0, U_x=U_y=V_x=V_y =0, V = 0, or N = 0.015 s^{-1}, respectively.

Figure 15. The time-height plots for rays initiated with (a) $k_0 = l_0 = 2\pi/400$ km^{-1} and (b) $k_0 = 2\pi/400$ km^{-1} and $l_0 = 0$ at 6 km above MSL over Patagonian every 2 h. The time interval between two adjacent dots along each ray path is 1 h.

Manuscript (non-LaTeX)
Click here to download Manuscript (non-LaTeX): andes_wave_figures1-5.doc

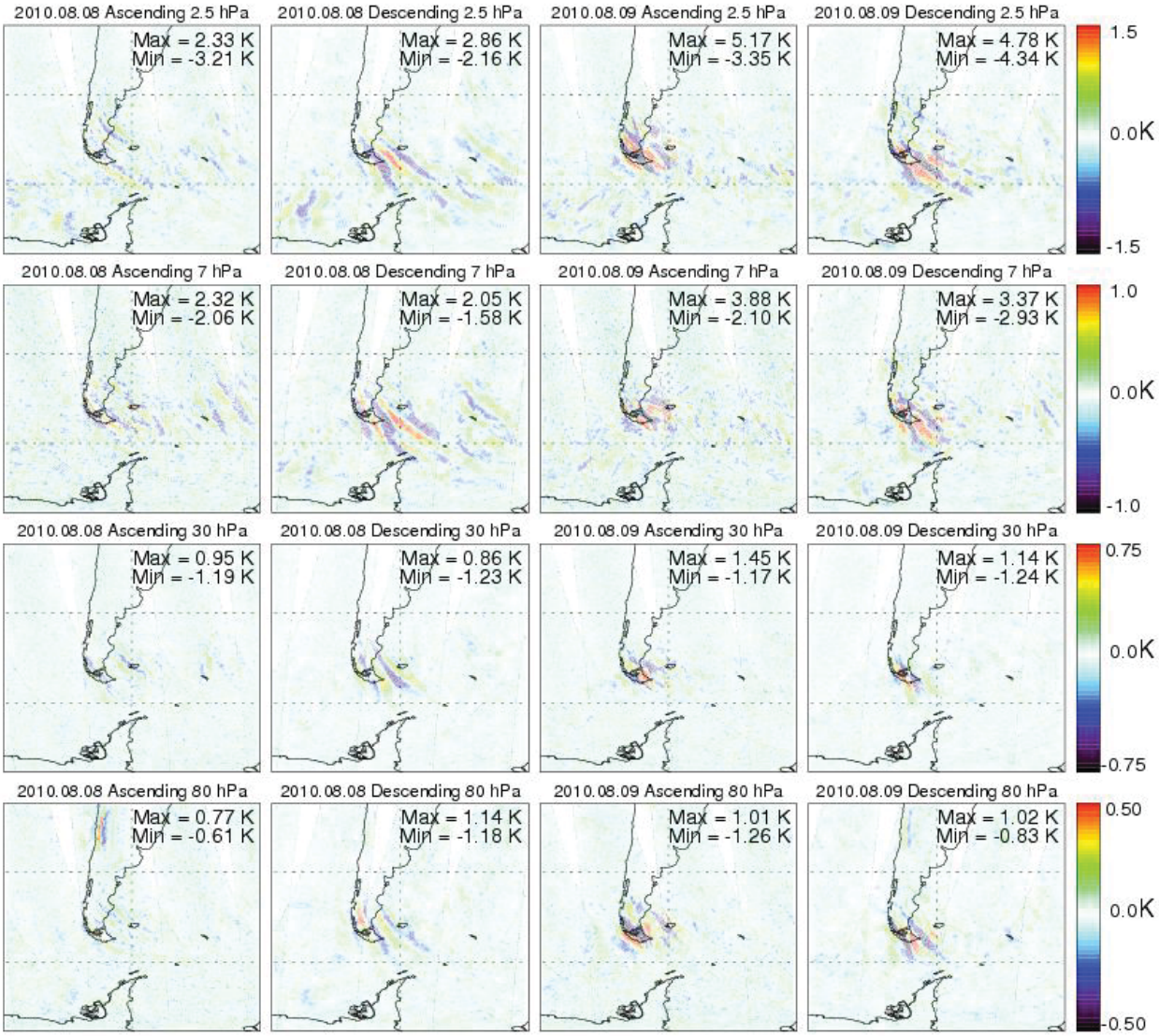

Figure 1. Small horizontal scale brightness temperature anomalies (K) extracted from multichannel AIRS radiances peaking at the indicated altitudes of (from bottom to top) 80 hPa, 30 hPa, 7 hPa and 2.5 hPa (see Table A2 and accompanying discussion of Gong et al. 2012 for channel details) from the ascending and descending overpasses of the southern Andes region on 8 and 9 August 2010. These perturbations were isolated by fitting and then subtracting along-track radiance structure with horizontal scales >600 km, including systematic limb effects as a function of scan angle (Eckermann et al. 2006). A 3x3 point smoothing of radiance anomalies in neighboring footprints was applied in these plots to suppress channel noise and accentuate the geophysical wave perturbations.

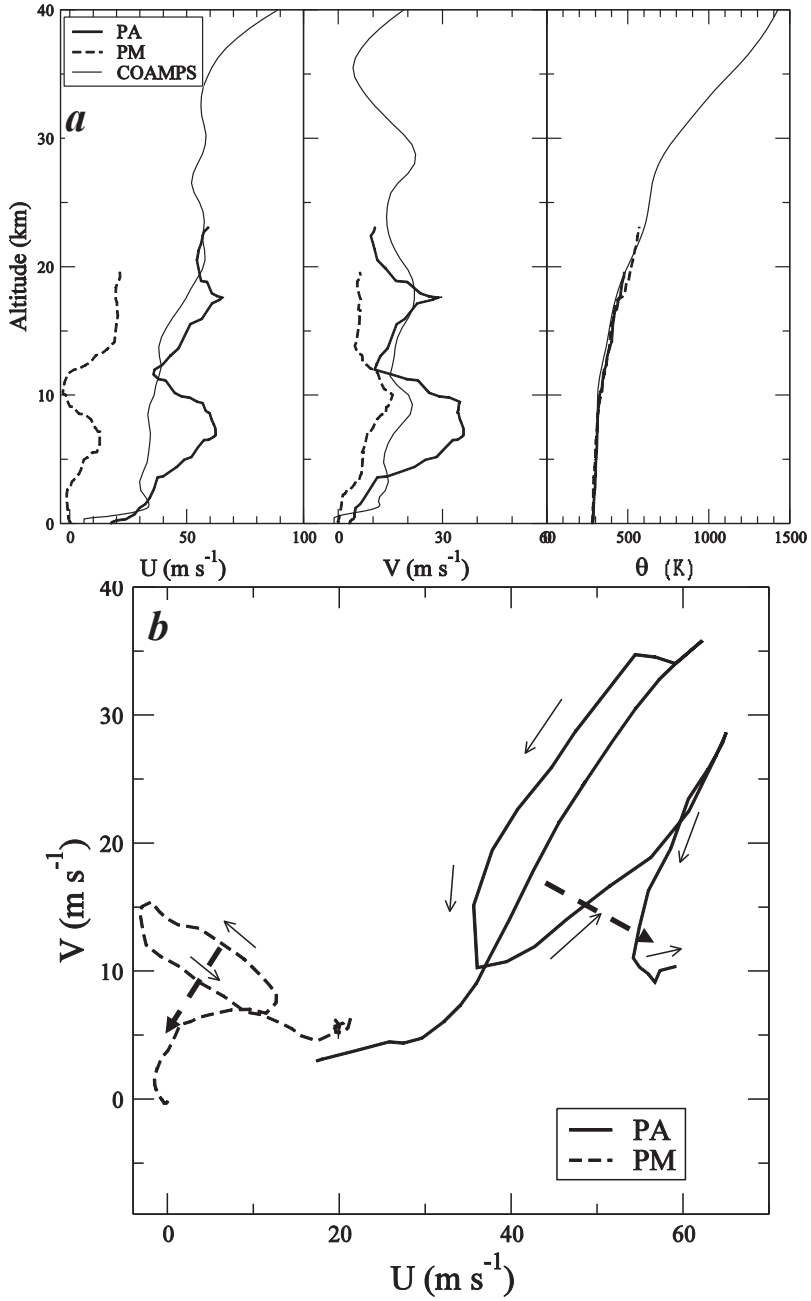

Figure 2. Wind and potential temperature profiles from the 1200 UTC, 9 August 2010, Puerto-Montt (PM, 41.43S, 73.10W; solid) and Punta-Arenas (PA, 53.00S, 70.85W; dashed) soundings are shown in a). The corresponding hodographs are plotted in b) with the rotating direction of the primary loop for each sounding indicated by thin arrows. The bold-dashed arrows indicate plausible wave vector directions.

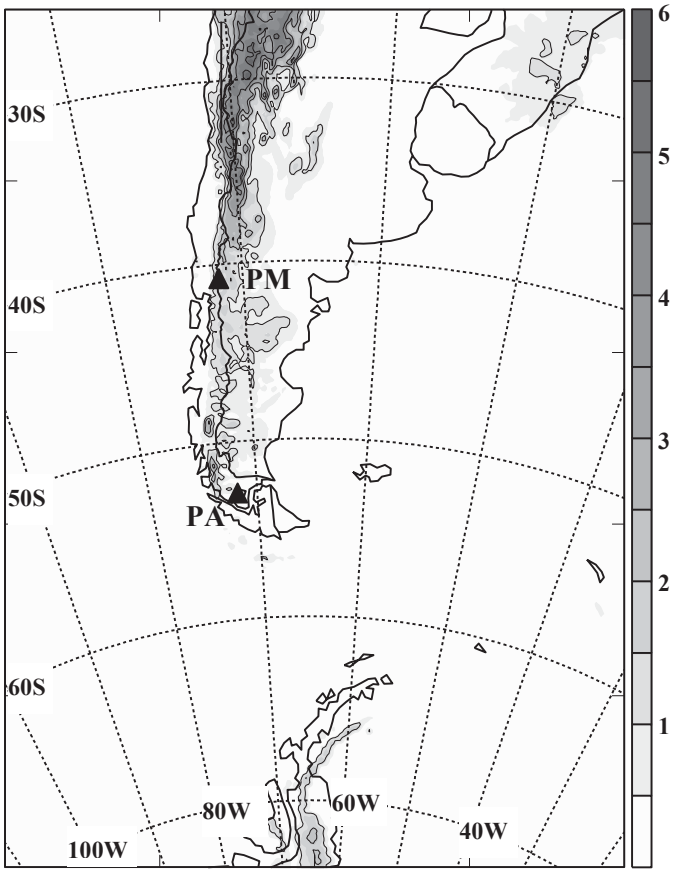

Figure 3. Topography in the 15-km grid domain is shown in gray shading (interval= 0.5 km). The locations of the two radiosonde stations, Puerto Mont (PM) and Punta Arenas (PA), are indicated by triangles.

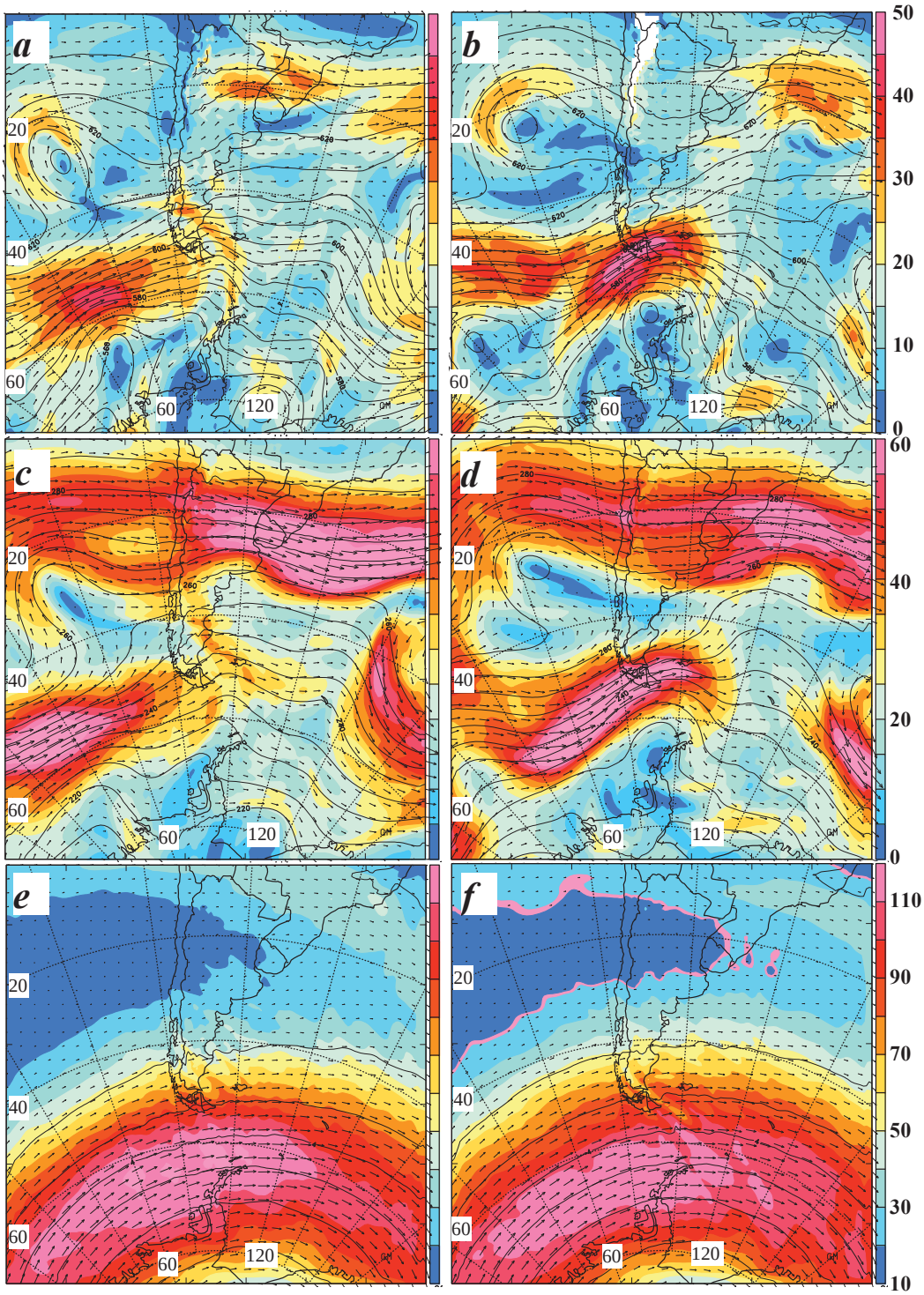

Figure 4. Synoptic flow patterns from the 45-km grid. The horizontal wind speed (color, increment is 5 m s^{-1} for a-d and 10 m s^{-1} for e-f), wind vectors, and pressure contours at the 4-km, 10-km, and 35-km levels valid at 1200 UTC 8 August 2010 are shown in the left panels. The corresponding graphics for 1200 UTC 9 August 2010 are shown in the right panels. The pressure contour intervals are 5 hPa for the 4-km and 10-km levels and 0.5 hPa for the 35-km level.

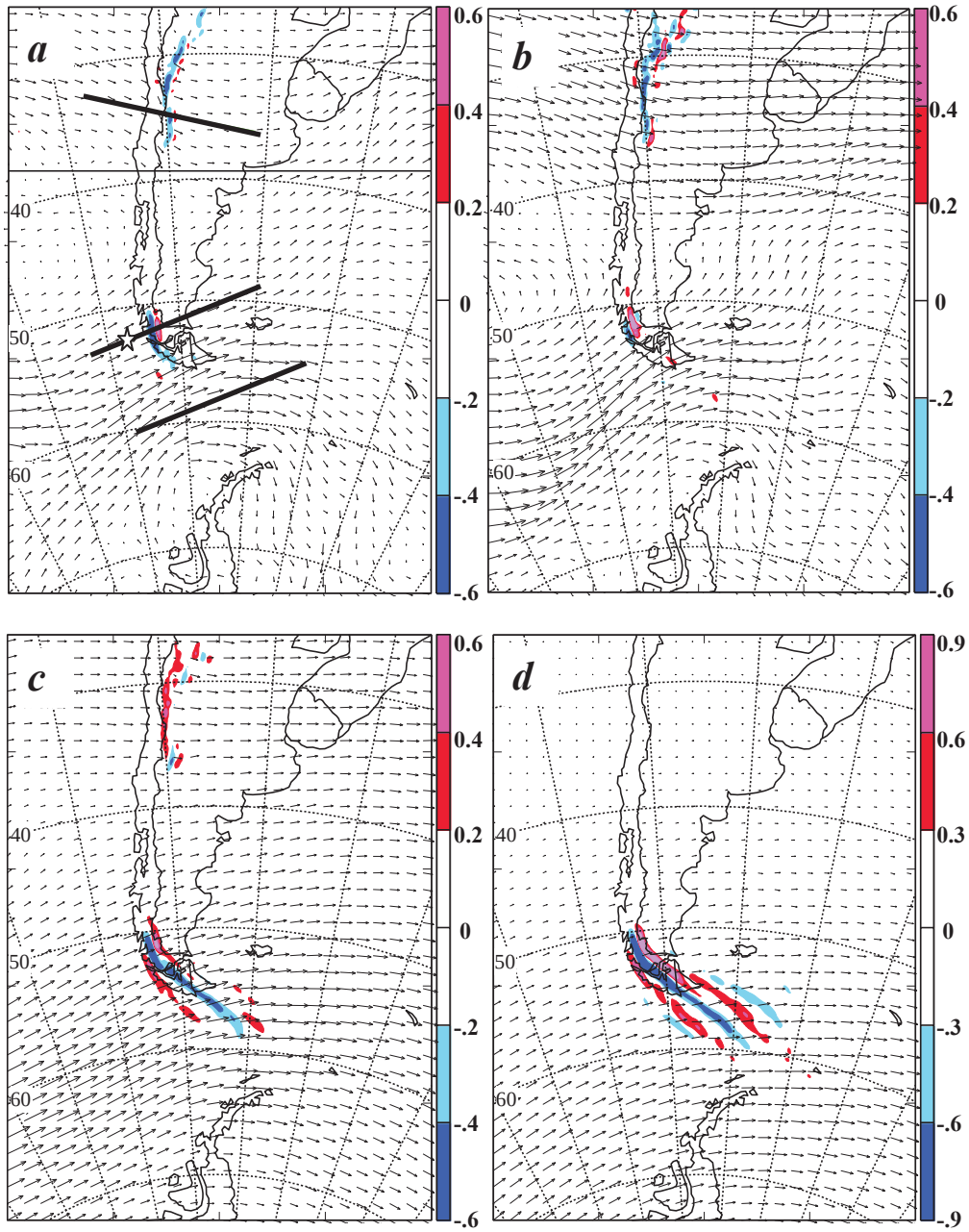

Figure 5. Plan-views of the vertical velocity (color, increment is 0.2 for a-c and 0.3 m s^{-1} for d) and horizontal wind vectors at a) 4, b) 10, c) 17, and d) 30 km ASL, respectively, valid at 1200 UTC, 9 August, 2010. The three bold lines and star in a) indicate the locations of the three cross-sections shown in Fig. 6 and the location for time-height diagram in Fig. 7c, respectively.

Manuscript (non-LaTeX)
Click here to download Manuscript (non-LaTeX): andes_wave_figures6-9.doc

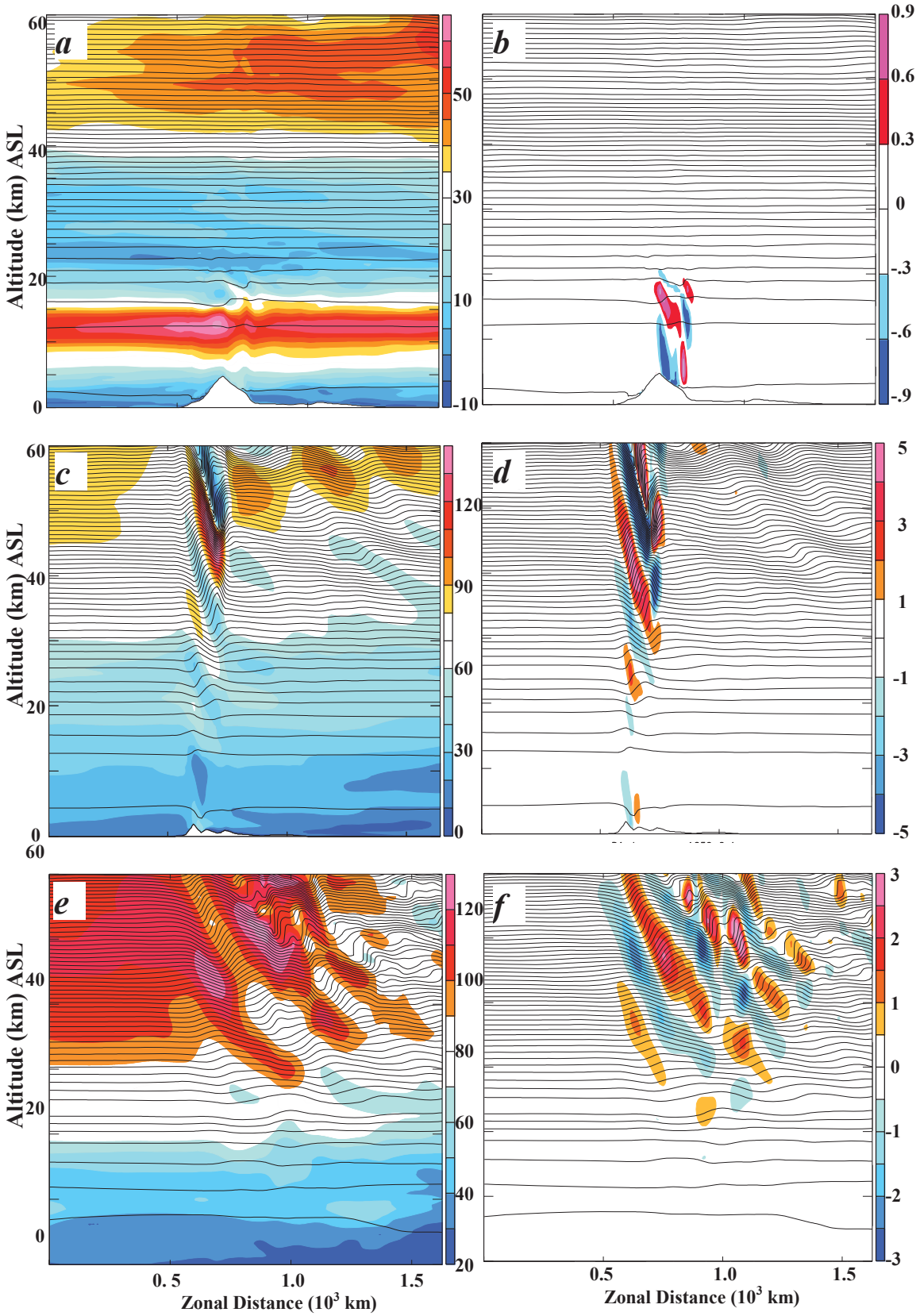

Figure 6. Cross-sections of zonal (i.e., *u*, left, increment is 5 for a and 10 m s^{-1} for c and e) and vertical (i.e., *w*, right, increment is 0.3 for b, 1 for d and 0.5 m s^{-1} for f) wind components oriented across the Central Andes (top), Patagonian (middle), and Drake Passage (bottom, see Fig. 5a for locations) valid for 1200 UTC, 9 August 2010.

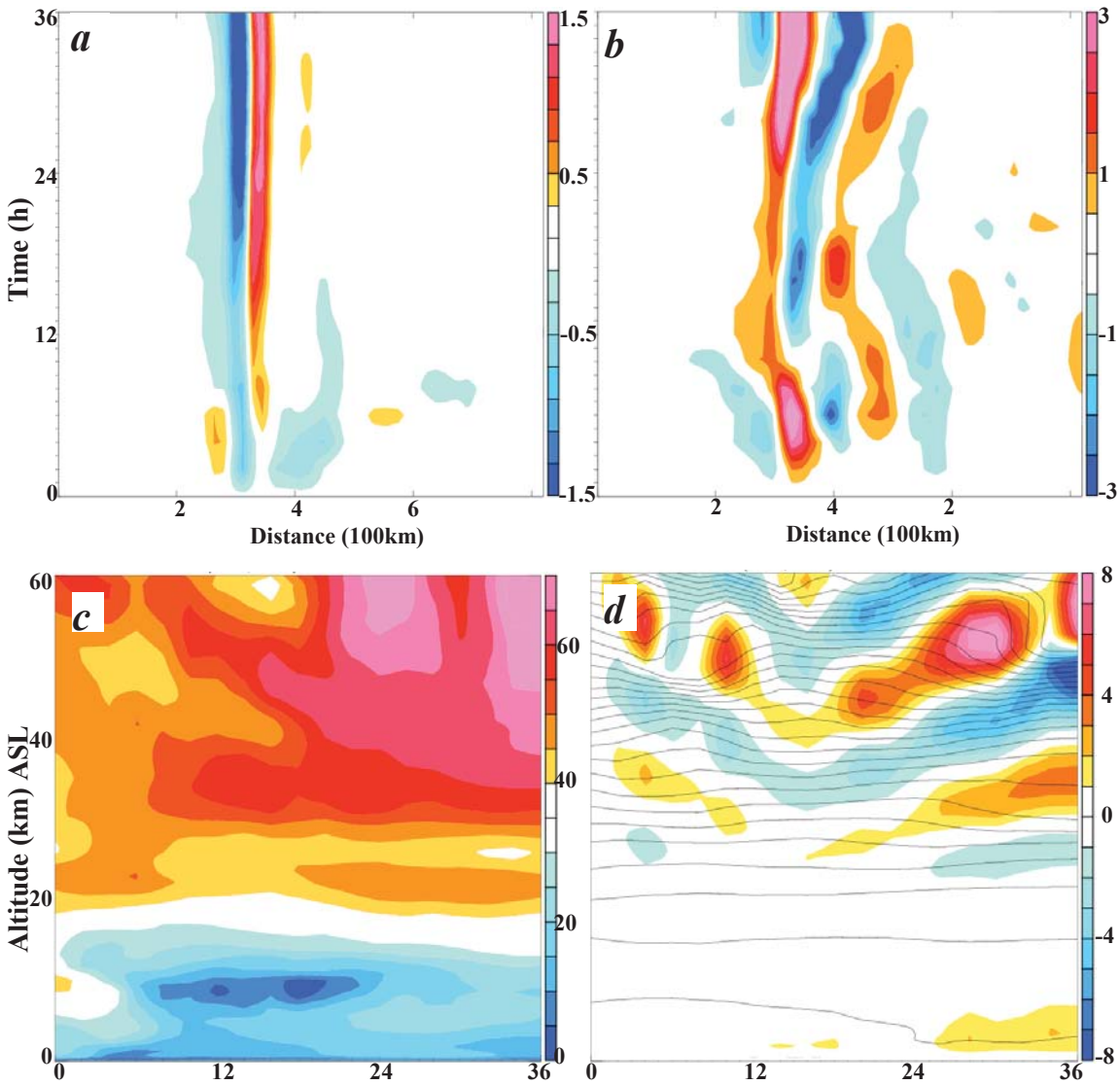

Figure 7. Shown in a) and b) are distance-time (i.e., Hovemöller) diagrams of the vertical velocity at 4 km (incr.: 0.2 m s^{-1}) and 40 km (incr.: 1 m s^{-1}) ASL along the same cross-Patagonia section as in Figs. 6c-d (but over a shorter distance). Shown in c) and d) are time-height diagrams of the upstream zonal winds (incr.: 5 m s^{-1}, see Fig. 5a for location) and vertical velocity (incr.: 1 m s^{-1}, superimposed with the corresponding isentropes, incr.: 100 K) in the leeside.

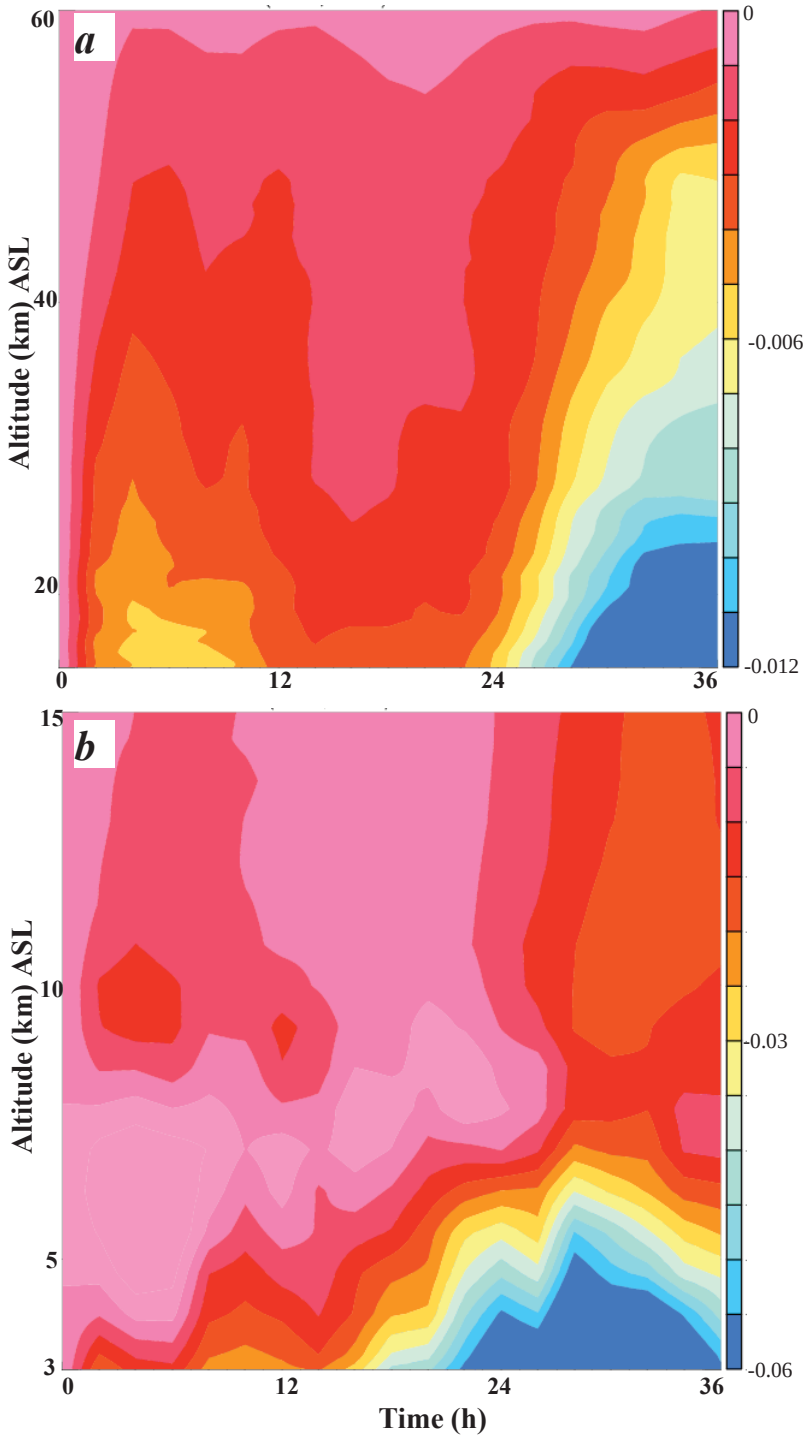

Figure 8. Time-height plots of the vertical flux for the zonal momentum (i.e., F_x) averaged over the southern Andes and Drake Passage. For the troposphere (lower), the range is from -0.06 to 0 with an increment of 0.005 N m^{-2}, and for the stratosphere, the range is from -0.012 to 0 with an increment of 0.001 N m^{-2}.

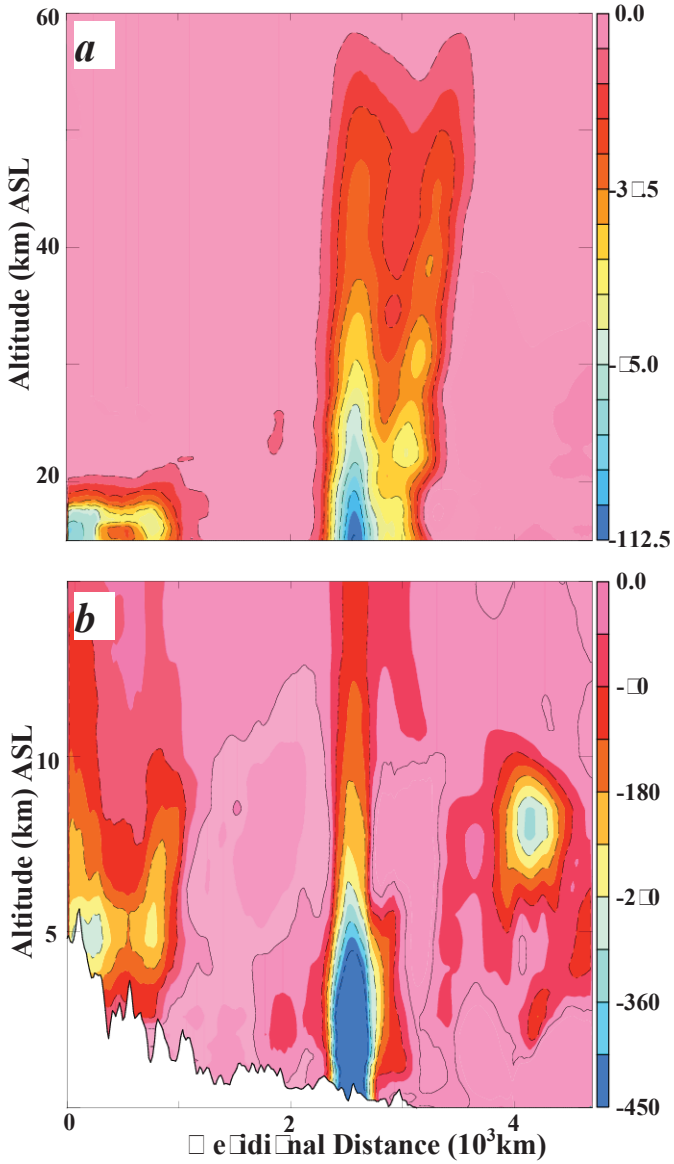

Figure 9. Vertical cross-section of vertical fluxes of the zonal momentum for the lowest 15 km (lower) and between 15 and 60 km ASL (upper) valid at 0000 Z (a and c) and 1200 Z, 9 August 2010, respectively. The grayscale intervals are 7.5×10^{3}N m^{-1}for a) and 45×10^{3}N m^{-1} for b).

Manuscript (non-LaTeX)
Click here to download Manuscript (non-LaTeX): andes_wave_figures10-15.doc

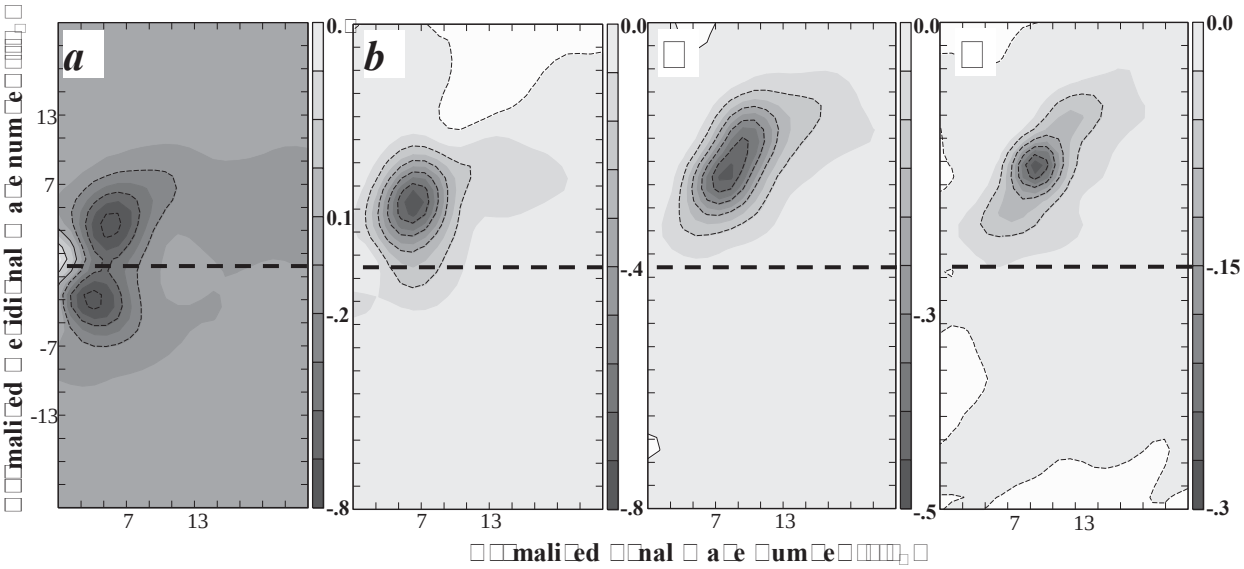

Figure 10. The vertical flux of zonal momentum spectra (i.e., $\hat{F}_x(k,l)$) at 12, 20, 45 and 55 km above MSL valid at 1200UTC, 9 August 2010 are shown in grayscale (intervals are 0.15, 0.08, 0.05, and 0.03 N m^{-2}) and contours (intervals=0.3, 0.16,0.1, and 0.06 N m^{-2}; negatives are dashed). The horizontal and vertical axes correspond to zonal and meridional wave numbers. Only wave numbers in the range of $1 \le k \le 23k_m$ and $-21k_m \le l \le 21k_m$ are shown, where $k_m = 2\pi/(256\Delta x)$.

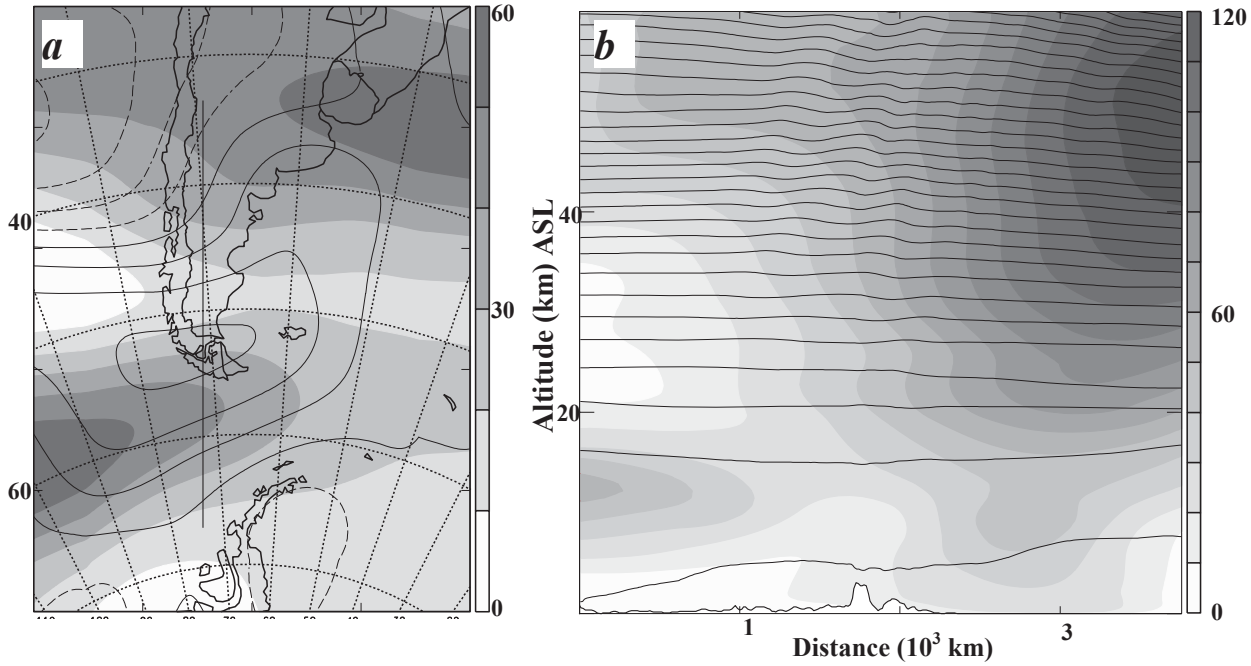

Figure 11. Plan-view of the 24-h average true zone (grayscale, incr. = 10 m s^{-1}) and meridional (contour, incr. = 5 m s^{-1}, negatives are dashed) wind components at 10 km ASL is shown in a). Panel b) shows a vertical cross-section of the true zone wind component (grayscale, incr. = 10 m s^{-1}) and isentropes (incr. = 100 K) oriented north-southly approximately along the Andes ridge (location indicated by the solid line in a).

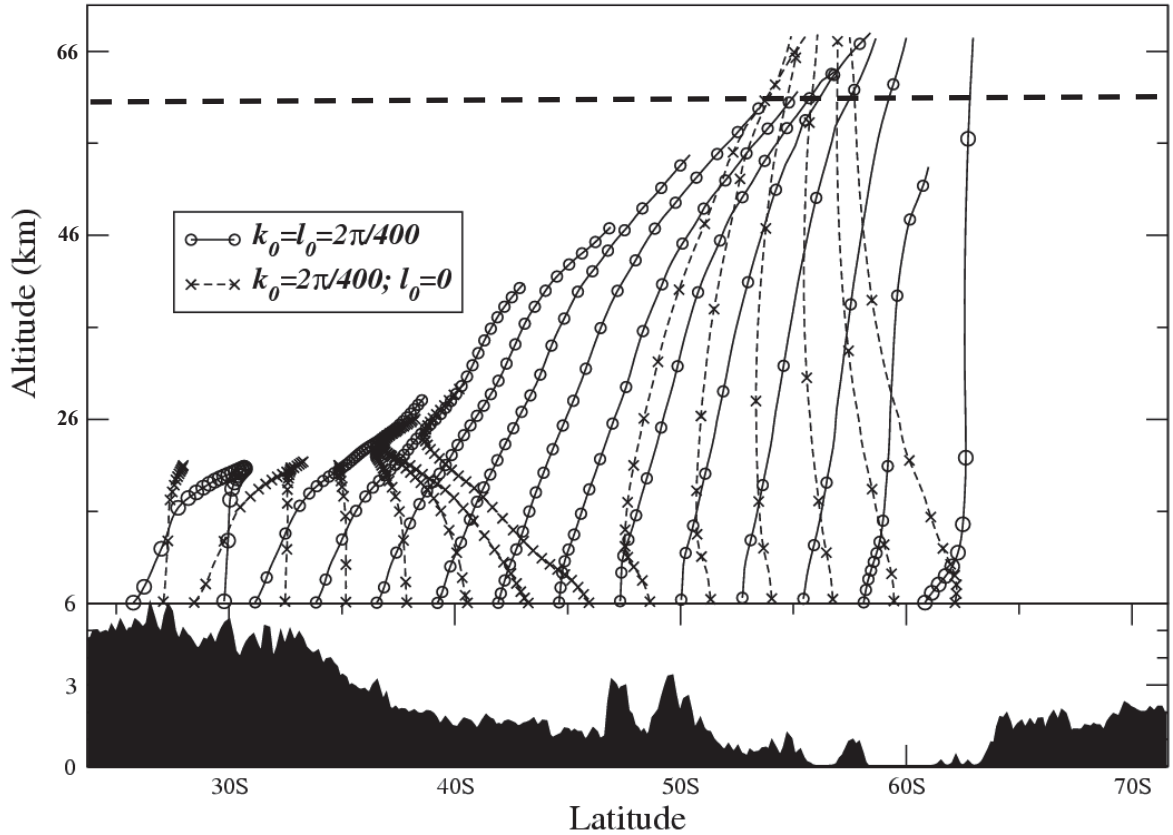

Figure 12. Ray paths in the y-z plane calculated using the 24-h average COAMPS winds and buoyancy frequency are shown. These rays are initiated at x=105 (in grid points) and z = 6 km with $k_0 = 2\pi/400$ (km^{-1}). Two sets of ray paths are shown, he solid rays correspond to y = 20n (n=1, 2, 3…) in model grid points and $l_0 = k_0$, and the dashed rays correspond to y=20n + 10 and $l_0 = 0$. The time interval between two adjacent symbols (i.e., circles for set 1 and crosses for set 2) is 1 hour. The maximum terrain height is shown below. The dash-bolded lines here and in Figs. 13-15 indicate the bottom level of the model sponge layer.

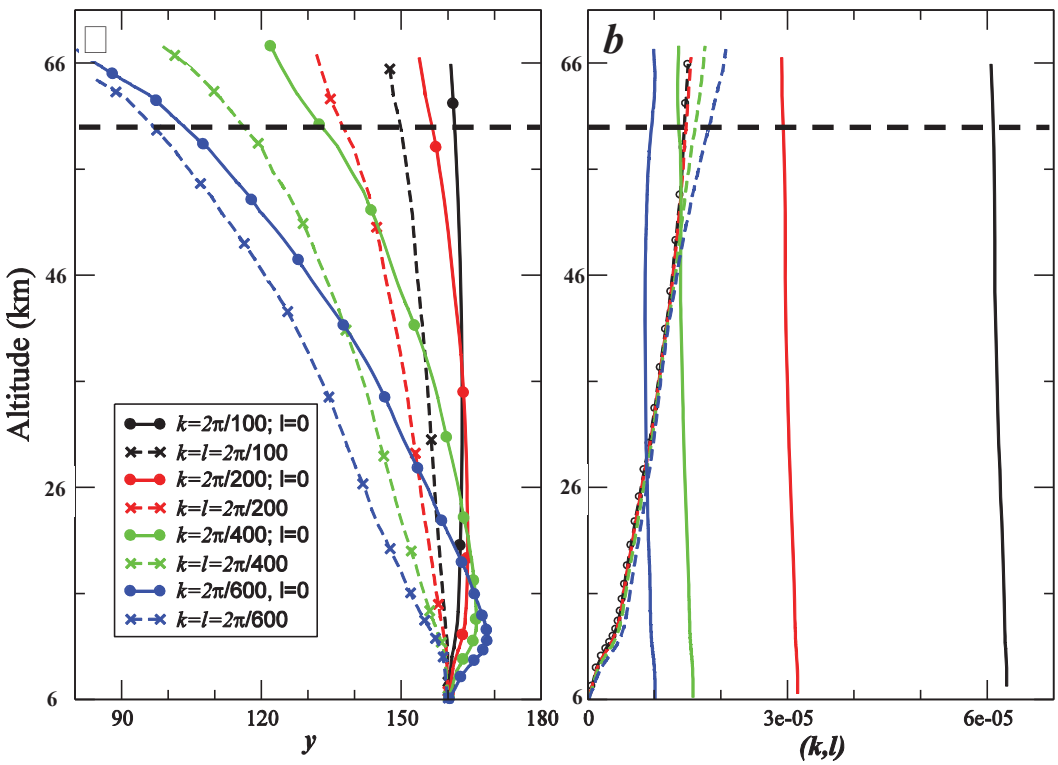

Figure 13. Ray paths in the y-z plane (a) and horizontal wave numbers (k□l) (b) along each ray path for four pairs of wave packets with k_0 = 2π/100, 2π/200, 2π/400, and 2π/600 (km^{-1}) and l_0 =0 and k_0, respectively. In (b), the k□(solid) and l□(dashed) curve are shown in the same color as in a) for each wave packet.

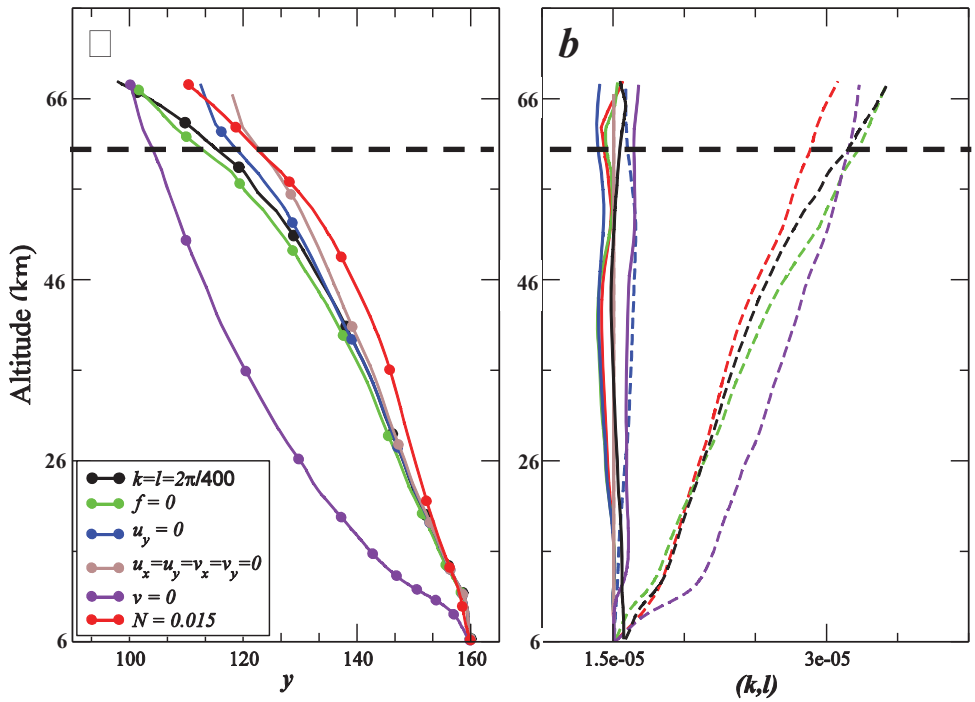

Figure 14. Ray paths in the y-z plane (a) and wave numbers (b) are shown for $k_0 = l_0 = 2\pi/400$. The other five pairs of curves correspond to paths and wave numbers calculated from the identical parameters except for f=0, U_y =0, U_x=U_y=V_x=V_y =0, V = 0, or N = 0.015 s^{-1}, respectively.

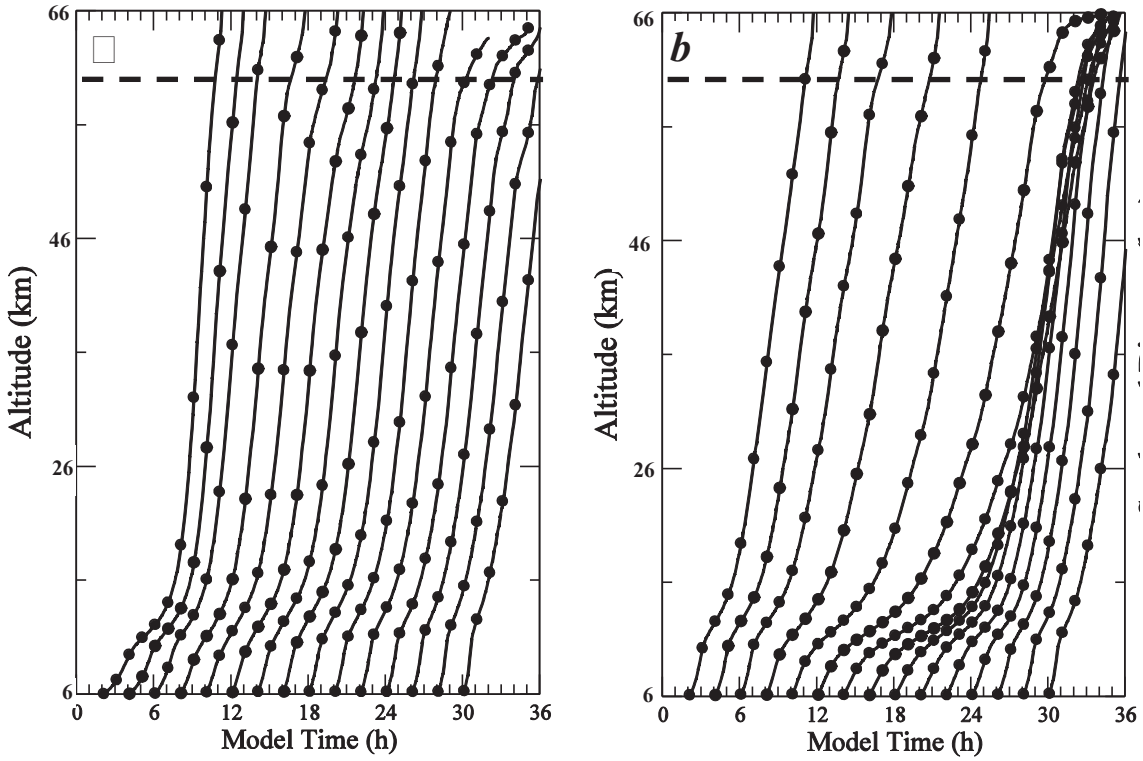

Figure 15. The time-height plots for rays initiated with (a) $k_0 = l_0 = 2\pi/400$ km^{-1} and (b) $k_0 = 2\pi/400$ km^{-1} and $l_0 = 0$ at 6 km above MSL over Patagonian every 2 h. The time interval between two adjacent dots along each ray path is 1 h.